Structural Bridges and Mechanically-Driven Spatial Patterning Along Mitotic Chromosomes

Chu, L.[1], Liang, Z.[1], Mukhina, M.[1], Vincenten, N.[1,2], Fisher, J.[1,3], Cribb, J.[4], Hutchinson, J.[5] and Kleckner, N.[1]*

1. Department of Molecular and Cellular Biology, Harvard University, Cambridge, MA. 02138
2. current address: Department of Genetics, Harvard Medical School, Boston, MA, 02115
3. Redbud Labs, Research Triangle, NC. 27709
4. Micro6 LLC, Durham, NC. 27705
5. School of Engineering and Applied Sciences, Harvard University, Cambridge, MA. 01238

*Corresponding author and lead contact. kleckner@fas.harvard.edu

Keywords:
mechanical effects, chromosomes, spatial patterning, mitosis, sister chromatids, chromosome compaction, torsional stress, chromosome axes

SUMMARY

Spatial patterning is a fundamental feature of biological and physical systems. Here, by high resolution fluorescence microscopy, we discover that the structural axes of individualized sister chromatids are linked by mini-axis "bridges" and that these bridges are dramatically evenly spaced. These findings reveal a new basic feature, and define the first robust example of spatial patterning, for mitotic chromosomes. Three roles for bridges are identified. Overall, the structural sturdiness and even spacing of bridges allows chromosomes to support the turbulent events of chromosome compaction, spindle formation and anaphase segregation. Analysis of chromosome axis paths reveals that even spacing arises by a mechanical process, as in physical systems. Axial torsional stress plays a prominent role, linking this mechanism to classical theories of elastic rods. A two-tiered process emerges. These findings suggest that mechanically-driven even spacing will be a general feature of chromosome organization and function in ways yet to be discovered.

INTRODUCTION

Chromosomes can usefully be considered as mechanical objects whose organization and functionality are governed by internal and external forces and resultant stresses. In support of this perspective, we have previously shown that the mitotic chromosomal program comprises alternating periods of bulk chromatin compaction and expansion whose properties suggest that they correspond to periods of accumulation and release of stress as mediated by installation and removal of molecular and catenation tethers (Kleckner et al., 2004; Liang et al., 2015).

One of the most attractive features of mechanical systems is that they provide an automatic built-in possibility for spatial patterning. As mechanical objects, chromosomes should be subject to such patterning. For example, if a system is under stress, a local stress-promoted will necessarily result in a local reduction in stress. In a complex system, that effect will tend to spread outward, thereby producing a self-limiting domain of reduced stress. If a second stress-promoted change occurs, it will tend to occur outside of this domain. And as additional events occur, they will tend to "fill in the holes" between the domains resulting from previous events, ultimately tending to produce a pattern of evenly-spaced changes (Kleckner et al., 2004; Figure 1A). However, at present, there is no robust example of spatial patterning within, along or among mitotic chromosomes, irrespective of mechanism. In the present study, using high resolution live cell fluorescence imaging of diverse mammalian cells, we identify such patterning and show that it does, in fact, arise by a mechanical process.

We first describe our discovery that individualized sister chromatids are linked by structural bridges from the time of sister individualization at late prophase through their progressive loss at anaphase. These bridges represent a new basic feature of mitotic chromosomes and a completely new aspect of sister chromatid connectedness. Furthermore, definition of molecular components reveals that these bridges are miniature structural axes. Thus, these bridges are mechanically robust and therefore specifically suitable for roles in protecting chromosomes from the external forces and turbulence characteristic of spindle formation and in constraining internal forces that may arise during chromosome compaction. Three such roles are defined.

Secondly, we show that these inter-sister bridges are dramatically evenly spaced along the chromosomes, at all stages from prophase to onset of anaphase. This discovery represents the first example of spatial patterning along/among mitotic chromosomes. By analysis of axis paths, we have elucidated the mechanism of this patterning: even spacing arises by a two-tiered mechanical process that prominently involves accumulation and relief of torsional stress along the chromosome axes. Among other implications, these results imply that the previously-defined concept of chromosome progression by alternating cycles of stress and stress relief (above) can apply not only to bulk chromatin but also to events along chromosome axes. In addition, these findings, for the first time, link a basic biological process to classical physical theories of elastic rods from the turn of the previous century. We propose that the observed effects provide a new general paradigm for thinking about global chromosome behaviors.

RESULTS

Background. High resolution fluorescence imaging has defined the basic morphological progression of chromosomes from the time they first appear as discrete units at the classical stage of mid-prophase to the time of separation onset at anaphase (Figure 1B; Liang et al., 2015 and Nagasaka et al., 2016; see also Gibcus et al., 2018). Mid-prophase chromosomes are assembled into co-oriented sister linear loop arrays, with loops emanating asymmetrically from a robust structural axis (further discussion below). Sister chromatids then individualize during a late prophase transition stage, characterized by splitting at both the axis and chromatin levels, with loops reorganized into a more radial disposition around the individual axes. Chromosome length does not change and, overall, chromosome volume increases (Liang et al., 2015). This transition, which occurs much earlier in the program than previously suspected, is enabled by synergistic loss of cohesins and topological catenations. Then, from prometaphase to late metaphase, individualized chromosomes become shorter and fatter in preparation for anaphase separation.

This progression has the characteristics predicted for chromosome stress cycling at the bulk chromatin level: compaction, with installation of tethers, to give a high energy stressed state; expansion via release of tethers in which stress is alleviated and previously stored energy is used to promote sister individualization; followed by another round of compaction (Figure 1B; Liang et al., 2015)

These recent findings raised two further questions. First, mid-prophase chromosomes, and their axes, were found to exhibit sharp bends and kinks (Liang et al., 2015; Figure 1C left), the origin and significance of which are unknown. Second, since sister chromatids individualize so early in the program, they must somehow retain a regular, parallel, side-by-side relationship for the entire period of prometaphase and metaphase (Figure 1C right; Gimenez-Abian et al., 2004; Video 1). This in turn implies that a regular relationship must be maintained despite the turbulent and disruptive effects of spindle formation and, internally, of progressive chromosome compaction. The only features implicated in sister associations after prophase are residual cohesins, which are present at the inter-sister interface, plus topological catenations which, however, are known at least partially dynamic (Gimenez-Abian et al., 2004; Piskaldo et al., 2017). The discoveries described below emerged from further investigation of these issues.

Sister Chromatids are Linked by Inter-axis Bridges from Late Prophase to Anaphase. TopIIα localizes along the axes of mammalian chromosomes from prophase through anaphase (Liang et al., 2015; Maeshima and Laemmli, 2003; Gomez et al., 2013; Gimenez-Abian et al., 2002). By high-resolution visualization of TopIIα we discover that sister chromatid axes are linked by discrete bridges along their lengths, from the time of sister individualization onward. Bridges emerge at late prophase and persist into/through anaphase (Figures 1D-1F and S1A; below). TopIIα bridges are observable in diverse mammalian cell types as visualized by diverse methods, i.e. 3D imaging in living pig (LLC-Pk) cells expressing GFP-TopIIα (Figure 1D) and by immunostaining of fixed whole cells of muntjac (DM87), human (HeLa, HCT116) and pig (LLC-Pk) (Figures 1E, 1F and S1B) and of diverse spread cell preparations (Figure S1C; below), irrespective of ongoing changes in chromosome stage, and in all analyzed

cell lines (details below). Other components are described below. The identified bridges comprise a new basic feature of mitotic chromosomes and are the first feature of sister connectedness to be identified since the discovery of cohesin proteins more than years ago.

Bridges Exhibit Even Spacing and, thus, One-dimensional Spatial Patterning. Bridges are very evenly spaced, with the same inter-bridge distance of ~400nm, at all stages from appearance to disappearance. This feature is visually apparent (Figure 1D-F) and has been quantitatively documented for TopIIα signals, and for signals of other bridge components, in living and/or fixed cells of muntjac, HeLa and pig (Figure 2ABC; Figures S1-S3; Figure S5). Notably, moreover, bridge spacing remains constant even as chromosome axes become progressively shorter (Figure 2BC). Correspondingly, the number of bridges along the chromosomes decreases in parallel with decreasing chromosome length on both an individual and a per-nucleus basis. These observations are important for two reasons. First, even spacing in a feature that is predicted to be important for many global chromosomal processes (Introduction) and this is the first robustly-defined example of this pattern for a mitotic chromosomal event. Second, even spacing implies the presence of one-dimensional spatial patterning. The mechanism of such patterning is of fundamental interest.

We have previously shown that individualizing sister chromatids first form small "bubbles" of axis splitting which then progress to fully-split axes (Liang et al., 2015; Figure 2D). We now see that bubbles also tend to be closely and evenly-spaced, at the same ~400nm distance as bridges (Figures 2E, 2F top). Correspondingly, bubble lengths are slightly smaller than inter-bridge distances and are extremely uniform (Figure 2F bottom). These considerations imply that the primary outcome of one-dimensional spatial patterning is an array of evenly-spaced bubbles, with bridges then emerging at the positions between those bubbles (Figure 2G).

Inter-axis Bridges are Miniature Axes. Bridges are also detected by visualization of other axis components. Where tested, these components colocalize with TopIIα

bridges (Figures 3A-3J and S2A-S2I). By prometaphase, bridges contain not only TopIIα but also other known components of post-prophase axes, condensin II, condensin I, SMC5/6 and HMG1/Y, as shown by analysis of living and/or fixed cells of human, pig and/or muntjac (Figure 3A-G). In addition, bridges also contain the cohesin complex as defined by Rad21. Bulk cohesin is lost from the chromosomes during sister individualization at late prophase, both within the chromatin and along chromosome axes; however, a small residual amount of cohesin is known to remain at the inter-sister interface, and must be cleaved in order for sisters to separate at anaphase (Gimenez-Abian et al., 2004). We can now say that this residual cohesin is present on bridges. Correspondingly, removal of bridges requires cohesin cleavage (Figure S9B).

Inter-sister bridges also contain DNA, again as seen in living and/or fixed cells from various organisms (Figures 4A-4E). Moreover, differential staining of sister chromatid DNAs, by sequential labeling with EdU and BrdU, reveals that DNA from each sister emanates inward along each bridge (Figures 4F-4H). It is highly likely that bridges contain catenated sister chromatin loops (FIgure 4I), for two reasons. First, as described below, TopIIa activity is required in real time for disassembly of bridges. Second, in budding yeast, cohesin and SMC5/6 (both components of bridges, above) play direct roles in maintaining catenations between sister chromatids (Farcas et al., 2011). Third, Rad21/cohesin and topological catenations between sisters are known components of unsplit midprophase chromosomes (Liang et al., 2015; Nagasaka et al., 2016; Gimenez-Abian et al., 2002).

Cohesin and topological catenations between sister chromatid loops are basic features of unsplit mid-prophase chromosome axes (e.g. Liang et al., 2015), further suggesting that the inter-sister bridges evolved from unsplit axis segments and directly matching the finding (above) that bridges emerge from the residual unsplit prophase axis segments that remain between adjacent bubbles (Figure 2G).

Overall, these findings imply that bridges are miniature axes (Figure 4J). One important implication is that the two sister chromatid axes, as linked by bridges, comprises a

single, integral structural entity. Among other implicates, this integrated structure provides mechanical rigidity to the inter-sister relationship beyond that which could be afforded by elastic cohesin/catenation linkages between peripheral chromatin loops. This mechanical robustness allows them to both resist and constrain both external and internal forces (further discussion below).

Three Roles of Bridges Exploit Both Even Spacing and Structural Robustness.

Time-lapse imaging of prometaphase/metaphase chromosome TopIIα axes in living cells reveals that sister axes undergo dramatic fluctuations in shape when located both within, and far from, the main spindle assembly (Figures 5A and 5B). Since bridges are present throughout this period (e.g. Figures 1C-1E), we infer that they are responsible for maintaining this close alignment in the face of spindle forces. Structural robustness has a clear advantage over peripheral chromatin/chromatin connections, whose intrinsically elastic nature would not afford such closely parallel alignment. Even spacing is also advantageous. Bridges are spaced at an interval (~400nm) that is similar to or shorter than the length scale of the observed conformational fluctuations, thus ensuring regular coalignment regardless of the positions and natures of shape changes.

The existence of bridges has, furthermore, important potential implications for the process of longitudinal compaction. Chromosomes become progressively shorter (and fatter) from prometaphase to late metaphase, exactly the period when bridges are present. Given that they arise by a complex mechanism that is linked to sister individualization at late prophase (Figure 2D; below), it seems unlikely that bridges can arise *de novo* at later stages. Rather, it seems likely that bridges, once formed, remain present until they are progressively evicted during the compaction process or, finally, removed during anaphase (below). If the process of compaction is evicting bridges, then bridges must to some degree be constraining compaction. More specifically: it has been assumed for more than a century, and argued recently from molecular studies, that individual chromatids become shorter in end-to-end length by progressive helical coiling (e.g. Marsden and Laemmli, 1979; Gibcus et al., 2018.) However, the presence

of stable bridges would absolutely preclude regular helical coiling along the chromatid lengths, because each helical turn along one chromatid would force it to intertwine with the other chromatid into a plectonemic relationship, which is not observed and would not be compatible with clean separation at anaphase. These findings strongly suggest that the presence of bridges *between* sister chromatids also constrains the process of chromosome compaction *along* each chromatid, with specific implications to be determined. For any such effect, mechanical robustness will again be important, to constrain compaction forces. Even spacing will also be important to ensure that constraining effects act regularly along the chromosomes. In fact, the ~400nm spacing of bridges is of the same order as previously-defined protein abundance domains ("barber poles") (3and Laemmli, 2004) and certain molecularly-defined features (Gibcus et al., 2018).

Finally, timelapse imaging also reveals that bridges are the final target of programmed anaphase separation. During wide separation of sister chromatids, sisters "peel apart" progressively from their centromeres. Bridges are removed progressively at the separation fork, with bridges between telomere regions being the last to be removed (Figure 5C). Moreover, if TopIIα-inhibitor ICRF193 is added to cells undergoing this process, separation is stopped "in its tracks", with bridges present (Figures 5D and 5E). We infer that bridges are the actual molecular target of programmed (APC-promoted) anaphase segregation. Even spacing of bridges can promote this process by ensuring regular processive progression; the structural rigidity can ensure that sisters withstand spindle forces until the separation process has reached the appropriate site; and the structural complexity of bridges can ensure that separation is a fully-programmed event that rarely or never occurs "by accident". Onset of bridge removal also requires cleavage of bridge-associated cohesin (Figure S9B) and APC activity (Figure S10).

These images also reveal that peeling-apart is preceded by an abrupt separation of sisters globally along their lengths (Figures 5B and 5C, yellow; Figure S8). This process is visible in videomicrographs of whole living Haemanthus chromosomes (Video 1; Figure S8).

Spatial Patterning by a Mechanical Process. Even spacing of inter-sister bridges provides a unique example of spatial patterning within chromosomes. Such a pattern could emerge by a mechanical process, as must be the case in all physical systems, and as proposed for meiotic crossovers (Kleckner et al., 2004) or by a reaction-diffusion mechanism (Turing, 1952) as documented in multiple living systems (review in Halatek et al., 2018). We previously showed that unsplit prophase axes exhibit prominent deformations, e.g. bends and kinks (Liang et al., 2015; Figure 1C left; Figure 6A top; below). We suspected that these forms resulted from the effects of internal mechanical stress. In such a case, internally-generated forces would be trying to promote conformational changes which, however, would be resisted by chromosome organizational features. This situation, of constrained force, is the definition of mechanical stress (which is measured in force/area). If stress could then promote local sister splitting, with redistribution of the resulting relief of stress, multiple such events would give an array of evenly space bubbles, and then bridges in a paradigmatic stress and stress-relief process (Introduction; Figures 1A and 6A).

Prophase Axes Are Under Internal Mechanical Stress.

If bridge patterning results from a stress-and-stress relief mechanism, unsplit axes should accumulate stress (e.g. above).

Morphological Evidence. Four observations support our original intuition that axis deformations reflect the presence of mechanical stress. (i) The extent of deformation increases from mid- to late prophase, as seen by a decrease in the proportion of axes that are "smoother" rather than "more deformed" (Figure 6ABC), consistent with progressively increasing stress. (ii) As bubbles emerge, their adjacent unsplit regions tend to "more deformed" rather than "smoother", as if an entire chromosomal region comes under stress before giving rise to a bubble (Figure 6D). (iii) Blocking sister splitting by inhibition of TopIIα (with ICRF) results in hyperdeformation of axes (Figures 6E and S4). This effect confirms progressive accumulation of deformation (and, by

implication, stress). More importantly, it shows that, in normal cells, splitting alleviates deformation, in accord with our envisioned scenario.

Evidence from Axis Centroid Paths. Clear evidence for the presence of stress within axes emerges from detailed analysis of the paths of their intensity centroids. Prophase chromosome axes (Figure 6F; Liang et al., 2015) comprise a bulky protein/protein/DNA/DNA (catenation) meshwork from which chromatin emanates, mostly asymmetrically in one direction (Figure 6G) in a corresponding shape (Figure 6H). Importantly, the axis is a discrete entity mechanically, as well as morphologically (Houchmandzadeh and Dimitrov, 1999; Marko and Poirier, 2003), and thus suitable for supporting and transmitting stress. To further explore the nature of axis deformations, and thus possible sources of mechanical stress, we defined the paths of the intensity centroids for both axis (TopIIα) and chromatin (DAPI or H2B-mCherry) shapes (Figure 6I; STAR Methods). In brief, each shape was sliced along its length; the intensity centroid of each slice was determined; and the path of the centroid along its shape was defined. For axis centroids, tendencies for left- and right-handed helicity were determined and shown in red and blue, respectively, along the path (Figure 6I right).

The centroid paths of unsplit axes exhibit two distinctive features (Figures 6I-6L; Videos 2 and 3). First, axes exhibit helicity along their lengths, and this helicity comprises regularly alternating segments of left- and right-handedness, (Figures 6I-6L). Second, the paths are strikingly planar (Figures 6I-6L). The presence of helicity implies the presence of axial writhe, where writhe comprises the combination of bending and twisting. The purest form of writhe is a simple helix. Relative to a simple helix, the observed axial writhe is constrained, in two respects. First, alternation of left- and right-handedness implies the presence of a topological constraint, which affects the twisting component of the writhe. Second, the planarity of the axis path implies that writhe is anisotropic and, more specifically, that there is a constraint on the bending component of the writhe. These effects point to the existence of an underlying force for helicity that is impeded/constrained by chromosomal features. Such a situation, by definition, implies the presence of internal mechanical stress (force per unit area). Thus, the

observed axis conformation of constrained writhe provides very strong evidence for the presence of internal mechanical stress within unsplit axes. We note that when writhing occurs as mechanical instability, as we infer here, it represents a form of buckling.

A Novel Consensus Conformation.

T The observed features also reveal an interesting basic underlying consensus pattern along the axes: a regular series of evenly-spaced bends, with changes in handedness occurring at every other bend, at regular intervals of ~200nm (Figures 6J-6L right, turqouise and yellow dots; Figure 6N). We refer to this unique conformation as "sequential half helices of alternating handedness".

More specifically: (i) On average, segments of the two helical handednesses are of the same, relatively uniform contour length (~200nm ; Figures 6M and S6A). There is no consistent bias for left- or right-handedness as defined by either the relative numbers of segments of the two types (Figures 6M (insets)) or by the total contour lengths of each handedness (Figure S6B). These patterns thus imply a quite regular consensus substructure of alternating "LRLR" segments (Figure 6M bottom). (ii) Centroid paths exhibit prominent bends, which also tend to be regularly spaced (Figures 6I-6L). (iii) There is a correlation between the positions of bends and handedness changes, with handedness changes tending to occur at the positions of every other bend (e.g. Figures 6I-6K and 6L left; blue and yellow dots).

Three features of this conformation further confirm the presence and accumulation of internal stress within unsplit axes. (i) the bends and handedness changes are evenly spaced, regardless of their frequency (e.g. Figure 6K (i,iii) versus other examples in Figures 6I-6K). These effects strongly suggest that both features arise due to relief and redistribution of internal mechanical stress along the shape, with more frequent deformations reflecting accumulation of stress. (ii) The fact that bends and handedness changes tend to coincide is strongly suggestive of a cause and effect synergy between the two features, which can be expected from actively-induced writhe. (iii) The fact that deformation (and thus writhe) increases with time (Figure 6C) points strongly to

accumulation of writhe by an active process, with accompanying accumulation, relief and redistribution of stress giving the observed pattern of evenly-spaced alternating half-helices, rather than occurrence of a static process in which a writhed path is a passively-constructed architectural feature.

Axial Torsional Stress as Constrained by the Chromatin Matrix. The presence of constrained writhe implies the presence of stress within unsplit axes (above). But what is the underlying basis for this unique conformation?

Strikingly, the consensus structure for the axis path (Figure 6N) corresponds closely to that which emerges when an elastic rod is subjected to axial torsional stress. In such a system, the rod will twist up to a certain point and then, when the level of stress reaches the characteristic twisting limit of the rod, any additional twist is manifested as writhe (e.g. Figure 6O). This classical effect has been widely modeled, beginning with the classical analyses of Kirchhoff and Love (Kirchhoff, 1859; Love, 1927), and is seen to apply in both physical and biological (DNA) systems (e.g. Goyal et al., 2005, 2007). In the present case, the conformation of each individual ~200nm left- or right-handed axis segment corresponds to that observed when writhe first begins to develop, prior to development of a full helix (Figures 6O and 6P). Similarly, from a topological perspective, this conformation corresponds to the intermediate state that arises as twist is converted to helical writhe (Figures 6Q and 6P). We note that in the previously considered cases, stress arises either from external forces imposed at one end of a rod (Kirchhoff, 1859; Love, 1927; Figure 6O) or by internal growth of a rod with fixed ends (Gerbode et al., 2012). In the current case, as far as we know, chromosome ends are neither constrained nor subject to any imposed forces. We infer that torsional stress is both imposed and stored internally within the chromosome axes.

The further question, then, is how are the effects of torsional stress constrained to give the observed consensus shape (Figure 6N). Geometric anisotropy reflects a constraint on the bending component of writhe while the alternating handedness of helicity reflects a constrain on the twisting component (above). Coordinate analysis of axis and

chromatin centroid paths reveals that bending occurs only in the image plane (Figures 6L and S?). This relationship points to axis/chromatin matrix interplay as the source of the bending constraint. Specifically, it can be predicted bending perpendicular to the image plane of the shape would require compression of adjacent chromatin loops (Figure 6R) and this is intrinsically disfavored under *in vivo* solvent conditions (Marko and Siggia, 1997; Kleckner et al., 2004). The topological constraint on axial writhe, i.e. the constraint on axis twisting, could also reflect a constraint imposed by the supra-axial chromatin matrix, which would have to twist concomitantly. In accord with these possibilities, the chromatin centroid path is less deformed as compared to the path of the underlying axis (Figures 6I and 6L). This difference suggests that the chromatin matrix is responding to axis deformations in a muted way, as expected if it is tending to resist those changes. In summary: the twisting and bending constraints on writhe are both economically explained by resistance from the supra-axial chromatin matrix.

A Two-tiered Mechanical Process Explains Even Spacing. We envision that mechanical stress within unsplit axes can promote local axis splitting, with accompanying relief and redistribution of stress. Such events, occurring sequentially at multiple sites, would lead to formation of evenly-spaced bubbles and then bridges (above; below).

The presence of stress along unsplit axes is revealed by the presence of constrained writhe (above). In our envisioned scenario, that stress is used to promote axis splitting, i.e. bubble and bridge formation, with a concomitant reduction in stress. Therefore our scenario specifically predicts that split late prophase axes should exhibit less writhe than their unsplit precursors. This prediction is fulfilled. Parallel visualization of chromosomes at the two stages in living LLC-Pk EGFP-TopIIα cells (Figure 7A; Videos 4 and 5) reveals closely analogous axis paths, with alternating ~200nm segments of left- and right-handed helicity (Figures 7A and 7B). However, detailed analysis reveals that the axes of late prophase chromosomes exhibit less prominent curvature as compared to axes of unsplit chromosomes. This reduction is reflected in both the total distribution of curvatures at all positions and of average per-centroid curvature values

(Figure 7C). Reduction in curvature is diagnostic of reduced writhe which, in turn, implies that axis splitting is accompanied by a reduction of internal stress.

In fact, at a topological level, reduction of writhe is precisely the effect predicted if stress arises from axial twisting. Axial torsional stress will, by its intrinsic nature, tend to promote axis splitting: split axes, being thinner, will more easily accommodate/absorb twist. This effect will reduce the amount of unaccommodated twisting and will, therefore, result in a reduction in writhe, as observed.

Taken together, the above findings suggest a simple but elegant two-tiered mechanism for the emergence and one-dimensional spatial patterning of bridges along mitotic prophase chromosomes (Figure 7D). In this mechanism, the existence of the two tiers reflects temporal interplay between accumulation of axial torsional stress and programmed loss of inter-sister cohesion/catenation linkages.

Tier 1. Axial torsional stress is continuously generated within unsplit axes. Initially that stress creates a regular pattern of axis deformations, i.e. sequential half helices of alternating handedness. An important feature of this path is that the sites of handedness changes are discontinuities and thus should comprise local weak points or "flaws" along the axis (open circles open circles in Figures 7D top and 6N). These flaws are mechanistically analogous to the flaws present in the physical system described in Figure 1A).

Tier 2. Torsional stress then promotes axis splitting. Such splitting will occur preferentially at the positions the Tier 1 flaws (Figure 7D middle), analogously to the occurrence of "cracks" at the sites of flaws in the described physical system (Figure 1A). During prophase, as the level of torsional stress increases, chromosomes undergo molecularly-directed loss of cohesion/catenation linkages. Loss of these linkages reduce the level of torsional stress required for splitting and, therefore, will provides critical trigger for onset of that process. Multiple sequential splitting nucleations, each resulting in relief and redistribution of stress over a characteristic distance, will give evenly-spaced regularly-sized bubbles. Residual torsional stress at unsplit positions

between bubbles (below) may promote elongation of unsplit segments into bridges (Figure 7D bottom).

This scenario explains all of the basic observations presented above. Additional information suggests a corresponding morphological progression (Figures 7E and 7F). (i) Left- and right-handed axis segments alternate along unsplit axes every ~200nm (above; Figure 6M). Along unsplit axes, nucleation of splitting at a flaw sites (open circle; above), followed by redistribution of stress, explains the occurrence of bubbles of uniform size (~370nm; Figure 2F). (ii) Split late prophase axes exhibit the same ~200nm alternate handedness spacing as unsplit axes, with an average of one left- and one right-handed segment between each pair of adjacent bridges (Figure 7AB). This conservation of topology is explained by the fact that adjacent unsplit regions are present at the boundaries of each pair of left-plus-right segments, and thus each bubble (Figure 7E, grey arrows). These unsplit regions comprise topological barriers and thus will preclude topological adjustments between different splitting ~370nm regions. However, adjustments within each region can still occur, thus explaining the lack of direct linkage between handednesses on the two sisters (Figure 7B bottom). (iii) Bubbles often exhibit a concave conformation (Figure 7E, right). Such a conformation is expected if axes split by simple displacement within a left-plus-right handed segment (Figure 7E, left). (iv) Closely adjacent bubbles are twisted at the sites of residual unsplit regions (Figures 7F left and 2E). Untwisting (as driven by relief of residual torsional stress; above) could promote elongation of the residual unsplit regions into bridges (Figure 7F).

Finally, we note that our earlier findings regarding the mid- to late- prophase transition, (Liang et al., 2015), can also be integrated into the above scenario. We showed previously that release of inter-sister tethers allows redistribution of loops into a more radial conformation around each individualizing chromatin and that this effect tends to "push sister chromatids apart". This pushing effect should enhance the effects of cohesin/catenation loss by further reducing the threshold of force required for axial torsional stress to promote splitting. It is important to note, however, that transmission

of information *along* the chromosomes, which is the critical feature required for spatial patterning of bridges along split axes, can only be achieved by accumulation and local relief and redistribution of an effect that confers longitudinal communication, e.g. axial torsional stress, which must therefore be the critical trigger for local splitting.

Summary. Evenly-spaced bridges between sister chromatids arise by a mechanically-promoted stress-and-stress relief process driven by axial torsional stress. A two-tiered process is defined. Progression through the two tiers results from temporal interplay between accumulation of such stress and programmed loss of inter-sister cohesion/catenation linkages.

DISCUSSION

The findings presented above provide a new perspective on how mitotic chromosomes evolve to meet the unique functional requirements of post-prophase spindle formation and chromosome compaction. They also confirm and reinforce the existence and fundamental importance of mechanical forces within chromosomes, in several respects.

Robust Sister Connections After Prophase. We identify a new chromosomal feature (and, more specifically, a new feature of sister chromatid connectedness): the axes of individualized sister chromatids are linked by evenly-spaced bridges that comprise miniature axes. Thus, the two sister chromatid axes, as linked by bridges, comprises a single, integral structural entity. The structural robustness and even spacing of these bridges are specifically appropriate to their roles in constraining and transducing mechanical forces specific to the period at which they occur.

Bridges provide physical stability to the sister couple as they align on the mitotic spindle and, then, are likely the ultimate target of anaphase segregation. In addition, most interestingly, bridges are predicted to significantly constrain longitudinal compaction

along each chromatid. Specifically: the presence of bridges is not obviously compatible with regular helical coiling, which has been the dominant concept for more than a century, up to and including very recent studies (Gibcus et al., 2018). This potential implication remains to be explored.

Spatial Patterning in Chromosomes. Even spacing of bridges represents the first robustly-defined example of spatial patterning in mitotic chromosomes. We show that this pattern arises by a unique mechanical stress-and-stress relief process. Given the intrinsic mechanical nature of chromosomes, it can be expected that analogous mechanically-based patterning effects remain to be discovered for other aspects of chromosome organization and function. More specifically, even spacing should be an advantage for all basic features of chromosomes, fundamentally because it ensures that global events will occur in a spatially regular way along their lengths. In fact, DNA replication initiation (Lebofsky et al., 2006), axial chromosome protein domains (Maeshima and Laemmli, 2003), and disposition of G1 chromosomes in discrete territories (Cremer and Cremer, 2010), among other features, all tend to be evenly spaced. Mechanically-based spatial patterning may underlie these and/or many other fundamental features of chromosomes.

Patterning by a Two-tiered Mechanism Driven by Axial Torsional Stress. We show that spatial patterning of bridges arises by a two-tiered mechanism, driven by axial torsional stress. The two tiers represent sequential stages that result from temporal interplay between accumulation of such stress and programmed loss of inter-sister cohesion/catenation linkages.

The molecular events responsible for generating torsional stress within axes remain to be defined. It can be noted, however, that: (1) important components of unsplit axes are TopIIα, condensin II and cohesin (Liang et al., 2015), three ATP-utilizing molecules that have the capacity to reconfigure chromosomes (reviews in Skibbens, 2019; Wang, 2002) and (2) important components of cohesins and condensins complexes are HEAT repeat proteins, which tend to be solenoidal (e.g. Groves and Barford, 1999; Yoshimura

and Hirano, 2016) and which we have shown previously to be elastic transducers of mechanical stress (Grinthal et al., 2010).

The specific mechanical process defined for bridge spacing is, to our knowledge, unique in a biological system. Moreover, the observed effects, for the first time, link a basic biological process to classical physical theories of elastic rods from the turn of the previous century (Kirchhoff, 1859; Love, 1927). Interestingly, however, the process defined here differs importantly from the classical physical case of an elastic rod because the observed effects arise internally within the system and because they reflect complex interplay between the chromatin matrix and the axis ("rod"). Further analysis of bridge formation thus provides a unique opportunity to explore basic physical principles in a biological context.

In the physical context, we also note that periodic patterns of bends and alternating handedness have been observed previously in elastomer bilayers where the internal stress is generated by bonding together layers with different initial stretches and then relaxing the average stretch by reducing the equal and opposite forces at the ends in a controlled manner (Liu et al., 2014). However, in that situation, as in the case of plant tendrils (Gerbode et al., 2012; above), the observed effects require tethering of the object at its ends and the handedness changes are smooth "perversions" rather than discrete bends.

Summary. Detailed analysis of mitotic chromosome morphogenesis has revealed a new general feature of sister connectedness, identified the existence of robust spatial patterning within chromosomes, and elucidated a unique mechanism whose mechanical nature is likely to have broad implications and applicability.

ACKNOWLEDGEMENTS

The authors thank T. Hirano, K. Maeshima, J. Ellenberg, G. Gorbsky, M. Kanemaki, Peter Cook, David Lleres, J.V. Shah and J-M. Peters for reagents, M. Stouf for Matlab scripts, all Kleckner laboratory members and Denise Zickler and Guido Guidotti for helpful discussions, and J. Henle for help with manuscript preparation. This research was supported entirely by a grant to N.K. from the National Institutes of Health (GM-025326).

AUTHOR CONTRIBUTIONS

L.C. and Z.Y. collected data. Z.Y. discovered bridges and performed initial analyses; L.C. confirmed and extended these initial findings and elucidated the mechanical basis for bridge emergence. N.K., L.C., Z.Y., N.V., M.M and J.H. analyzed data. J.F. and J.C. created the algorithm for centroid path analysis. All authors participated in preparation and/or editing of the manuscript.

DECLARATION OF INTERESTS

The authors declare no competing interests.

FIGURE LEGENDS (TEXT)

Figure 1. Mitotic chromosomes and TopIIα bridges. **A.** Even spacing of mechanically-promoted events illustrated for a physical system. Left: a beam coated with a thin brittle film containing weak points ("flaws"). When heated, the beam expands, leading to stress along the film/beam interface which ultimately give rise to cracks at the positions of flaws. Right: A crack results in local relief of stress which redistributes outward in both directions, thereby precluding occurrence of additional cracks nearby. A second crack will occur outside of this domain of stress relief. Analogously, additional cracks will fill in the holes between prior crack domains, leading to even spacing (not shown). Adapted from Kleckner et al., 2004. **B.** Mitotic chromosomes progress from prophase to metaphase in three stages (from Liang et al., 2015). **C.** Left: prophase chromosomes are morphologically single units that exhibit dramatic shape deformations.

Right: at metaphase, sister chromatid arms are still closely aligned. 3D images of living whole muntjac DM87 cells for DNA (Hoechst staining) and fixed whole cell TopIIα axes (right) (Liang et al., 2015 and unpublished). **D-F.** TopIIα bridges link split sister axes from late prophase through anaphase. **(D)** Living pig LLC-Pk EGFP-TopIIα cells; **(E,F)** fixed whole cells stained with anti-TopIIα antibody in muntjac DM87 **(E)** and HeLa **(F)**. Dashed bars are 5μm and solid bars are 1μm. Additional examples in Figure S1.

Figure 2. TopIIα bridges are evenly spaced and arise from evenly-spaced bubbles. **(A, C top)** Even spacing of bridges along late leptotene chromosomes. **(A)** SIM images of DM87 nuclei immuno-stained for TopIIα; source nuclei in Figure S4B. **(C, top)** Quantification inter-bridge distances for LLC-Pk GFP-TopIIα chromosomes in live cells. Distributions of distances were fit by a gamma distribution (STAR Methods). Values of the data mean and the shape parameter from gamma fit are given. **(B, C below)** Even spacing of bridges throughout prometaphase and early and late metaphase, at ~400nm, as at late prophase (**panel A**). Illustrated **(B)** and quantified **(C)** for LLC-Pk GFP-TopIIα chromosomes in living cells. Analogous results for all stages are seen for other cell types in fixed cell images of TopIIα and DNA bridges (Figure S5). **(D)** A whole muntjac DM87 nucleus undergoing the late prophase transition, fixed and immunostained for TopIIα, exhibits unsplit axes, bubbles of axis splitting and split axis segments linked by bridges. Additional single bubbles examples in Figure S4B. **(E,F)** Bubbles of axis splitting are evenly and closely spaced. This is apparent by visual inspection and confirmed by quantification (e.g. brown and blue). Closely adjacent bubbles are separated by the same distance as bridges (mean ~ 0.4 μm; **F top**). Bubbles are nearly as long as the inter-bubble spacing (mean = 0.37 vs 0.4 μm, **F bottom vs F top**), in accord with close spacing. **(G)** Data in **panels (C, E and F)** imply that unsplit axes give rise to evenly-spaced bubbles, with bridges then arising in the short remaining unsplit regions that link adjacent bubbles (text).

Figure 3. TopIIα bridges also contain other known structural axis components. **(A-C)** Bridges contain condensins II and I as visualized for chromosomes in living cells of DM87 (**A**) and HeLa (**C**) carrying GFP-tagged kleisins β and γ respectively (also known as CapH2 and CapH). In (**A**), all stages are shown, documented by whole nucleus chromosome visualization with H2B-mCherry. **(B,D)** Condensins II **(B)** and I **(D)** colocalize with TopIIα along bridges as seen by co-immunostaining of chromosomes in fixed HeLa and/or HCT116 cells. **(E,F)** SMC6 occurs along bridges in colocalization with TopIIα as seen by co-immunostaining of DM87 chromosomes. **(G)** Architectural protein HMG1/Y localization to bridges is seen by immunostaining of DM87 chromosomes. **(H-J)** Rad21 cohesin colocalizes with TopIIα along bridges as seen by co-immunostaining of HeLa cell chromosomes **(H).** Quantification documents the two signals' colocalization along the inter-chromosomal region (yellow dashed lines in lower images of panel **(H)**), as shown in panel **(J)**. Dashed bars are 5μm and solid bars are 1μm. Corresponding whole nucleus images for all panels plus visualization of condensin I kleisin γ in living DM87 cells are presented in Figure S2.

Figure 4. TopIIα bridges also contain DNA. **(A-E)** Bridges are observed by visualization of DNA or chromatin of chromosomes in living and fixed cells as indicated. Direct visualization of overlap with TopIIα is shown by co-staining **(D, E).** Chromosomes in **(B)** and (**C**) are at pre-anaphase where global separation of sister chromatids (below) makes bridges more apparent. **(F-H)** Bridges contain DNA emanating from both sisters. **(F,G**) Sister chromatid DNAs were differentially stained by sequential exposure to low toxicity F-ara-EdU and BrdU followed by further incubation in the absence of either label to allow an additional round of DNA replication and then exposure to a mitotic kinesin Eg5 inhibitor (STLC) to allow accumulation in metaphase (details in STAR Methods). **(H)** Individual bridges (defined by total staining; arrows in bottom panel) can each be seen to involve DNA signals emanating towards one another from both sisters (dots in top panel). Additional weaker DNA linkages likely reflect nonspecific loop catenations. **(I)** Bridges are proposed to include catenated sister chromatin loops. **(J)** Bridges as

defined in **Figures 1-3** contain post-prophase axis components (green) plus cohesin (red) and (proposed) sister loop catenations. Whole nucleus images for **(A-E)** are presented in Figure S3. Dashed bars represent 5μm and solid bars are 1μm.

Figure 5. Bridges between chromatid axes shepherd the sister couple through post-prophase stages to ensure their regular segregation.

(A, B) Live cell imaging of LLC-Pk EGFP-TopIIα chromosomes shows that sister chromatid axes remain closely parallel throughout the dynamic motions of metaphase chromosomes, even when not closely associated with the main spindle (as in panel **(B)**, enlarged images below). Additional examples in Figures S7A and S7B. **(C)** Live cell time-lapse imaging of LLC-Pk EGFP-TopIIα cells elucidates the stages of anaphase (text). Sister chromatids undergo progressive global separation during the minute prior on onset of movement of sister centromeres to opposite poles (t= - 1'0" to 0'0"; yellow line) with slight but discernible separation in the preceding 30" dashed line); quantification in Figure S7C. Analogous progressive global separation is seen in living Haemanthus chromosomes (Figure S7D, S7E; Video 1). Bridges remain present until the moment of wide separation (arrow; see also Figures 1C and S1A), suggesting that their removal may be the rate-limiting step of programmed separation. Thereafter, chromosome ends remain oriented towards one another (t = +3'0"), suggesting the presence of residual invisible linkages (e.g. DNA catenations). **(D)** Visualization of live DM87 chromosomes illuminated with H2B-mCherry reveals that addition of TopIIα inhibitor ICRF-193 to chromosomes undergoing anaphase separation (STAR Methods) stops that process "in its tracks", with no loss of bridges or other discernible changes, consistent with the possibility that decatenation of bridge-associated sister chromatid loops is essential for programmed separation via bridge release. **(E)** Live HeLa cell chromosomes illuminated with H2B-mCherry, imaged at indicated times after addition of ICRF-193 as in panel **(D)**, showing robustness of bridges despite chromosome deformation due to arrest (full time course in Figure S9A). Anaphase separation also requires cohesin cleavage (Figure S9B).

Figure 5. Axis morphologies and centroid paths reveal mechanical stress patterns. **(A)** Morphological pathway of bridge emergence, illustrated by TopIIα axis shapes from DM87 nuclei. Increasingly deformed unsplit axes give rise to bubbles which then develop into mature late leptotene chromosomes with evenly-spaced bridges. Involvement of mechanical stress (text) also indicated. Source nuclei in Figure S4A. **(B)** Visual inspection of images of mid- and late prophase nuclei (e.g. panel **(B)**; Figure S4A) allows categorization of 1.2-1.5 μm unsplit axis segments into smoother and more deformed shapes according to whether the maximum deviation of the center line of the shape from a linear baseline is less or more than +/- 3 pixels **(B left** and **B right**, respectively). **(C)** The frequency of more deformed segments is higher in late prophase nuclei than in mid-prophase nuclei (defined by presence and absence of split axes, N=7 and 9 nuclei, respectively). Note: progression to more deformed shapes is likely greater than it appears because axes with increased deformation are constantly being converted to split axis forms. **(D)** In nuclei undergoing the late prophase transition, bubble regions that have an adjacent unsplit region(s) (bottom) were characterized for whether those regions were smoother or more deformed as defined in panel **(B)**. Most such adjacent unsplit regions are deformed, consistent with a link between deformation and splitting (text). **(E)** Living pig LLC-Pk EGFP-TopIIα cells were treated, or not, with TopIIα inhibitor ICRF193 at mid-prophase and imaged thereafter (STAR Methods; Figure S4C). After 20min, untreated cells were in post-late prophase stages (left) whereas treated cells were arrested in mid-prophase with unsplit axes that had become hyper-deformed (right). **(A-E)** Dashed bars are 5μm and solid bars are 1μm. **(F)** The mid-prophase cooriented linear loop configuration. **(G-I)** Representative mid-prophase axis shape and corresponding chromatin shape: Individually (**G, left)**; overlaid in 3D Pymol renderings to illustrate asymmetric emergence of chromatin at top (**G, right)**; in tilted orientations to illustrate corresponding lumpy shapes **(H)** and with centroids shown **(I).** For axis centroid paths, tendencies for left- and right-handed helicity are indicated in red and blue, respectively. Images in **(G-I)** are the same shape whoes centroids are shown in **Panel L(i). (J, K).** Representative centroid paths of unsplit axes, including those seen as shapes (i)-(iv) of panel **(A).** Shapes (i) and (ii) are "smoother"; all other shapes are "more deformed". Turquoise and yellow dots indicate bends without and

with accompanying handedness changes, respectively. Yellow arrowheads indicate sharp bends as in panel **(A)**. Shape perspectives chosen to reveal planarity of axis paths. See Video 2 for diverse perspectives of the centroid path in panel **(J)**. **(L)** Additional examples as in panels **(I-K)** with chromatin centroid paths also shown (green). See Video 3 for diverse perspectives of the centroids in panel **L(i)**. Notably: (a) chromatin centroid paths are smoother than axis paths; and (b) axis centroid paths are bent in the plane of the chromatin loops (yellow arrows). Examples in **(J, K and L (i))** are from DM87; examples in **(L(ii)** and **L (iii))** are from living LLC-Pk GFP-TopIIα cells. **(M)** Distributions of contour lengths of left- and right-handed segments of unsplit axes (above). Prominent peaks at ~200nm (arrows) pointing to a regular consensus alternation (below). Data are for living LLC-Pk GFP-TopIIα chromosomes. Total number of segments analyzed (Σ) were obtained from 14 chromosome axis images. The same patterns are seen in chromosomes from fixed whole muntjac cells immunostained for TopIIα (Figure S6A top). **(N)** The inferred consensus structure for unsplit axes: sequential half-helices of alternating handedness. Specifically: sequential ~200nm segments of alternating left and right handedness**,** each with a central bend, and a bend with associated change in handedness at each inter-segment junction. **(O-Q)** Individual segments along unsplit prophase axes have conformations that match those seen during initial conversion of excess torsional stress into writhe (text). Panel **(O)** shows the effects of increasing torsional stress on an elastic rod. The right end of the rod is restrained in rotation but is allowed to translate towards the left end. (Adapted from Goyal et al., 2007). **Panel (P)** shows the conformations that arise during topological conversion from twist to writhe (left; adapted from Wang and Cozzarelli, 1990). **Panel (Q)** shows the relationships among the consensus axis subsegment conformation (e.g. **panels J and N**), the initial deformation in **panel (O)** and the transitional topological conformation in **panel (P)**. **(R)** Planarity of axis bending along unsplit shapes may result from a differential constraint of chromatin pressure on bending perpendicular to the plane of the loops (left versus right).

Figure 7. Even spacing of bridges is driven by axial torsional stress in a two-tiered process. **(A)** Unsplit, splitting and fully split prophase chromosomes imaged in

parallel in living LLC-Pk EGFP-TopIIα cells (see Videos 4 and 5 for diverse perspectives of the mid- and late prophase shapes at top left and top middle). At all three stages, alternating segments of left- and right-handed helicity are apparent (**panel (O)**; additional examples in Figure S7A). Tilted version of one late prophase chromosome segment is shown without centroid to emphasize 3D undulations. **(B)** The distribution of segment lengths along the split axes of late prophase living LLC-Pk GFP-TopIIα chromosomes. A prominent peak is seen at ~200nm for both left- and right-handed segments (**panel B top**), just as in unsplit chromosomes (**Figure 6M**; Figure S6A top). Total number of segments analyzed (Σ) were obtained from 9 chromosomes, thus 18 chromatid axis images.The same features are also seen in fixed whole DM87 cells immunostained for TopIIα (Figure S6A bottom). Total number of segments of each handedness analyzed (Σ) were obtained from analysis of 9 chromosomes. Additionally, handedness at corresponding positions on sister chromatids is unrelated (Figure S6B), implying two types of average conformations (panel **B bottom**). **(C)** Split prophase axes show reduced curvature as compared to unsplit axes. Distribution of curvature magnitude for centroid paths of mid- (blue bars) and late (red bars) prophase chromosomes for all points of all analyzed paths (left) and per chromosome averages (right). Blue and red curves are kernel density estimation for corresponding distributions. Top and bottom panels show data for fixed whole cell DM87 chromosomes and live cell LLC-Pk TopIIα chromosomes, respectively. Curvature is calculated for arcs of 240 nm (STAR Methods). **(D)** A two-tier mechanical mechanism. Axial torsional stress first sets up an array of flaws along unsplit axes at positions of handedness changes (Tier I) and then, enabled by loss of cohesin/catenation likages, gives rise to evenly-spaced spaced bubbles and then bridges (Tier 2). **(E)** The scenario in **panel (D)** predicts that bubbles will exhibit a concave bubble geometry (left). Bubble morphologies match this prediction (right). **(F)** Adjacent bubbles are twisted relative to one another (top left; **Figure 6A(vii);** Figure S4C asterisk), consistent with the presence of residual torsional stress. Formation of bridges could be driven by this stress, which could drive "untwisting" followed by bridge emergence by extension of a residual unsplit axis segment (yellow) and concomitant straightening of axes across the bridge region (turquoise, brown).

FIGURE LEGENDS - SUPPLEMENTAL FIGURES

Figure S1. Additional examples of TopIIα bridges. related to text Figure 1. (A) Snapshots of chromosomes from living LLC-Pk EGFP-TopIIα cells at the indicated stages. Bridges are also seen in diverse types of fixed cell preparations and different cell types including **(B)** fixed whole LLC-Pk EGFP-TopIIα cells and **(C)** fixed spread DM87 chromosomes visualized with anti- TopIIα antibody.

Figure S2. Whole nucleus images for protein visualization plus bridges seen with condensin I kleisin γ in living DM87 cells. related to text Figure 3. (A-H). Whole nucleus images corresponding to individual chromosome images shown in text Figures 2A-2I. **(I)** Bridges visualized with condensin I GFP-kleisin γ in living DM87 cells.

Figure S3. Whole nucleus images for DNA visualization. related to rext Figure 4. (A-E) Whole nucleus images corresponding to individual chromosome images shown in text Figures 3A-3E, respectively. **(F)** Bridges at late prophase in *Bomeria multiflora* (9, 1936). **(G)** Bridges at late prophase in muntjac (Gimenez-Abian et al., 1995).

Figure S4. Additional images of late prophase morphogenesis. related to text Figures 2, 6 and 7. (A) Whole nuclei sources of individual chromosome images in text Figures 6A (i)-(ix) and 7E and 7F (orange boxes). **(B)** Whole nuclei sources of SIM images in Figure 2A. **(C)** Examples of bubbles from late prophase nuclei of DM87 fixed whole cells (top) and living LLC-Pk EGFP-TopIIα cells (bottom). Note figure 8 shape (*) and 3D deformations (**) as well as general tendency for "boat shape" (text Figure 7E). **(D)** LLC-Pk EGFP-TopIIα cells in mid-prophase were treated with DMSO, with or without ICRF-193, and imaged at indicated time points thereafter. Images in text Figure 6E are t=22min (DMSO+ICRF) and t=25min (DMSO).

Figure S5. Statistics of inter-bridge and inter-bubble distances. related to text Figure 2. Distances between adjacent bridges or between the centers of adjacent bubbles were measured in nuclei of the indicated cell types and stages. Number of distances measured for each case is given. Each distribution was analyzed by fitting to a gamma distribution (STAR Methods). CI = confidence interval.

Figure S6. Segment analysis: lengths, handedness and handedness relationships between sisters. related to text Figures 6 and 7. (A) Length distributions of left- and right-handed axis segments along mid- and late prophase chromososomes from DM87 fixed whole cells immuno-stained for TopIIα show the same features seen for axes in living LLC-Pk TopIIα cells as described in text Figures 6M and 7B. Data from analysis of 22 midprophase axis centroids and 8 late prophase images (thus 16 individual chromatid axis centroids). **(B, C)** Handedness relationships. Each position along the centroid of an unsplit or split chromosome axis comprises one pixel in the long axis of the shape (STAR Methods). Each such position is part of a left- or right-handed segment (red or blue, respectively, in text Figure 6I). The same living LLC-Pk GFP-TopIIα images were analyzed as in Figures 6M and 7B, respectively. **(B)** The total number of pixel positions of each handedness were determined for unsplit axes ("Mid-prophase") and for each of the two split axes of late prophase shapes. **(C)** Along late prophase axes, corresponding positions on sister chromatid axes can be of the same or opposite handedness.

Figure S7. Additional axis centroid examples. related to text Figure 6. (A) Multiple examples of axes and their centroids from living LLC-Pk TopIIα cells. **(B)** The centroid paths of axes and chromatin shapes tend to rotate around their shared geometric axis. A rotation of one handedness extends over a limited distance before reversing. Such rotation could be driven by chromatin pressure, which will tend to be alleviated by such rotation (Kleckner et al, 2004).

Figure S8. Sister chromatid axis alignment from prometaphase through anaphase. related to text Figure 5. (A) Parallel sister chromatid axis alignment

maintained along prometaphase chromosome (circled) despite dramatic shape changes, seen in LLC-Pk EGFP-TopIIα cells. **(B)** 3D views of a single sharply-bent prometaphase chromosome confirms continuous coalignment of sister chromatid axes. **(C)** LLC-Pk EGFP-TopIIα (pig) cells approaching and entering anaphase as shown in text Figure 5C. Quantification of distances between sister axes defines global arm separation. For each time point, lengths of red lines were averaged (left). Graph (right) shows that separation initiates ~2min before the time that sister centromeres can first be discerned to move towards opposite poles (t = 0) and results in approximately a doubling of inter-axis distance (~0.75-~1.4 μm). **(D, E)** Videomicrograph of Haemanthus chromosomes approaching and entering anaphase. Whole nuclei (top) with indication of sister centromere separation (turquoise, t=0) and selected pair of chromosomes (white box) shown in detail below (middle). Distance between the centers of one pair of separating sister chromatids was measured (bottom left). Analogously to the pig cells in **(C)**, these chromatids show global arm separation initiating ~1min before the time that sister centromeres can first be discerned to move towards opposite poles (t = 0). From Video 1 (Inoue and Oldenbourg, 1998; doi mk0780643001).

Figure S9. Anaphase separation requires cohesin cleavage and continuous action of Topoisomerase IIα. related to text Figure 5. (A) LLC-Pk EGFP-TopIIα cells in the middle of anaphase were treated with TopIIα inhibitor ICRF-193, which stops anaphase sister separation essentially instantly (see also Figure 5D and Figure 5E, which highlights the 44min and 60min time points of this experiment). **(B)** Bulk cohesin is released from prophase chromosomes at the mid-late prophase transition, leaving residual cohesin at the inter-sister interface; and cleavage of cohesin has been inferred to be required for anaphase sister separation, not only within centromere regions but also along chromatid arms (Gimenez-Abian et al., 2004). We show here that this interface cohesin is present on inter-axis bridges (text Figures 3H, 3I and 3J). These considerations predict that cohesin cleavage should be required for removal of bridges at anaphase. We tested this prediction using a HeLa cell line carrying non-cleavable Scc1, tagged by 9 myc epitopes, and expressed from a doxycycline (DOX)-inducible

promoter. This strain was exposed to DOX for 12 hours beginning in G1 and a cell in metaphase was then identified and imaged for 110min. In this protocol, progression of chromosomes beyond a prometaphase-metaphase configuration was completely blocked, with bridges remaining present, even as aberrant conformations and an abortive anaphase-like stage occur **(bottom panel).** In contrast, an isogenic wild type strain identified in metaphase and imaged analogously undergoes normal anaphase with concomitant loss of bridges **(top).** These results provide direct confirmation that anaphase sister separation requires cleavage of cohesin between chromatid arms and suggests that this requirement is due the requirement for cleavage of bridge-associated cohesin.

Figure S10. Global pre-anaphase sister separation and ensuing anaphase are blocked by earlier inhibition of the proteosome. related to text Figure 5. LLC-Pk EGFP-TopIIα cells were exposed to the proteosome inhibitor MG132 in early metaphase **(B)** in parallel with an untreated control **(A)** and monitored thereafter (STAR Methods). Treatment blocks global chromosomes with a prometaphase/metaphase configuration prior to pre-anaphase sister separation, which finally occurs after ~90min of MG132 **(B)**.

STAR METHODS

LEAD CONTACT AND MATERIALS AVAILABILITY

Further information and requests for resources and reagents should be directed to Nancy Kleckner at kleckner@fas.harvard.edu. This study did not generate new unique reagents. Cell lines transiently containing plasmids were not stored and can be reconstructed from previously-existing reagents.

EXPERIMENTAL MODEL AND SUBJECT DETAILS

Cell Lines. All cell lines are reported in the Key Resources Table. Human HeLa histone H2B-GFP cell line and pig LLC-Pk EGFP-TopIIα cell line were gifts from G. Gorbsky and J.Shah, respectively. HeLa-Scc1-9myc cell line and HeLa-Scc1-9myc-non

cleavable cell lines were gifts from J.M. Peters. The native DM87, HeLa, and HCT116 cell lines were gifts from P. Cook, J. Shah and M. Kanemaki, respectively. The Indian Muntjac mCherry-H2B cell line was constructed by transfecting DM87 cells with a pH2B-mCherry plasmid (a gift from Jan Ellenberg) and selecting with 1 µg/µl Geneticin. In some experiments, DM87 cells and HeLa cells transient co-express H2B-mCherry and EGFP-Kleisin-β or EGFP-Kleisin-γ after co-transfection with pH2B-mCherry and pEF1a-EGFP-Kleisin-β or pEF1a-EGFP-Kleisin-γ plasmids (the latter were gifts from Kazuhiro Maeh). The transient transfection protocol was executed using Effectene Transfection Reagent (QIAGEN) according to manufacturer's manual. All cell lines and plasmids are further described in the Key Resources Table.

Standard Growth Conditions. Cells were grown in Dulbecco's modified Eagle's medium (DMEM; Life Technologies) with 10% fetal bovine serum (FBS, VWR), 2 mM L-glutamine and 100 units/ml penicillin plus 100 µg/ml streptomycin (Life Technologies), at 37 °C with 5% CO_2 in a humidified incubator.

METHOD DETAILS

Synchronization and Inhibitor Treatments

For live cell imaging, pig cells were synchronized at G2/prophase boundary by incubating cells with 9 µM CDK1 inhibitor RO3306 for 20 hours (Vassilev et al., 2006) released by washing out the inhibitor with DMEM. Cells enter prophase within 1 hr after release. For DM87 cell snapshot studies, cells were synchronized with 2 mM hydroxyurea at the G1/S boundary for 20 hr. Cells reach mitosis ~7hr after release. For all HeLa cell experiments, cells were synchronized at the G1/S boundary by treatment with 2 mM thymidine for 24 hr and released by washing out the inhibitor with DMEM. Cells enter mitosis at ~7 hr after release.

For analysis of Scc1-9myc expression (Figures 3HI and S2G), cells were induced with 1 µg/ml of Doxycycline for 24-48 hr before fixation (Hauf etal., 2001).

For EdU labelling (Figures 4F and S3D), DM87 cells were synchronized with 2mM hydroxyurea for 20 hr, followed by release and treatment with 5 μM EdU for 7 hours and then fixed.

To obtain F-ara-EdU/BrdU labelled chromosomes, low toxicity F-ara-EdU was used (Neef et al., 2011). DM87 cells were cultured in the presence of 8 μM F-ara-EdU for 4 days and then synchronized at G1/S boundary with 2 mM hydroxyurea for another 24 hr. After release from hydroxyurea, cells were treated with 30 μM BrdU for 10 hr. Then these cells were subsequently released into F-ara-EdU/BrdU- free medium and cultured for 20 hr before fixation. To enrich more mitotic chromosomes for spread, cells were treated with 20 μM S-trityl-L-cysteine (STLC) for 12 hr.

For ICRF-193 treatment (Figures 5D, 5E, 6E, S4D and S9A), ICRF-193 was added to a final concentration of 2 μg/ml by adding to the medium volume in imaging dish an equivalent volume of medium containing 4 μg/ml ICRF-193, immediately prior to imaging

For MG132 and BI2536 treatment experiments (Figure S8), the protocol is the same as ICRF-193 treatment, but the final usage concentration for MG132 and BI2536 is 50 μM and 100 nM, respectively.

For imaging of Scc1-9myc-non-cleavable cells (Figure S9B), cells were transfected with pH2B-mCherry, further incubated for 8 hr, and then treated with 2 mM Thymidine for 20 hr to give synchronization at the G1/S boundary. At the time of release from arrest, Doxycycline was added to a final concentration of 1 μg/mL and cells further incubated and then imaged after an additional 12 hr.

Sample Preparation

Fixed Whole Cells. Whole cells were fixed by one of two methods: (1) Methanol fixation (Figures 1D, 2A, 2D, 2E, 3E, 3G, 4D, 6A, 6G-6I, 7A , 7E, 7F, S2F, S2H, S3D, S4A-4B, S4C bottom). Cells were rinsed in 1xPBS (Phosphate Buffered Saline) (137

mM NaCl, 2.7 mM KCl, 10 mM Na_2HPO_4, 1.8 mM KH_2PO_4, pH 7.4) and then fixed in pre-chilled 100% methanol for 20 min at -20°C. (2) "Pre-extraction" fixation as in (Liang et al., 2015; Hauf etal., 2001). Cells were rinsed with 0.1% Triton X-100 in HMK buffer (20 mM HEPES, pH 7.5, 1 mM $MgCl_2$, 100 mM KCl) and, after 1-2min, fixed by treatment either with pre-chilled 100% methanol for 20 min at -20°C (Figure 1C right) or with 3.7% paraformaldehyde for 10 min (Figures 1F, 3B, 3D, 3H, 3I, 4E, S1B, S2D, S2E, S2G and S3E). Following fixation, cells were rinsed with PBS, permeabilized with 0.01% (v/v) Triton X-100 in PBS (PBST) for 5 min and incubated in 5% BSA in PBST for 2 hr.

Spread Chromosome Preparations. Cells were collected after trypsinization, suspended in in hypotonic buffer of 50% culture medium in water for 5.5 min, and then fixed in freshly made pre-cold 3:1 methanol-acetic acid (Figures 3H-3I, S1C; Gimenez-Abian et al., 1995). Aliquots of the fixed sample were then dropped on slides and air-dried.

Immuno- and/or DNA staining For immunostaining, whole or spread cell preparations were incubated with the primary antibodies overnight at 4°C, or 1 hr at room temperature. After washing in PBST three times, cells were incubated for 1 hr at room temperature with secondary antibodies. As desired, cells were then stained with 1 µg/ml 4',6-diamidino-2-phenylindole (DAPI) in PBS for 10 min, or 0.1 µM YOYO1 in PBS for 10 min before mounting with ProLong Gold anti-fade reagent (Life Technologies).

Primary antibodies: monoclonal mouse anti-TopIIα (Millipore) at 1:100; polyclonal rabbit anti-hCapH at 1:50 (Novus); polyclonal rabbit anti-hCAPH2 at 1:500 (a gift from Tatsuya Hirano, Japan); rabbit anti-SMC6L1 at 1:50 (Abcam); polyclonal anti-HMG-I/HMG-Y(N-19) at 1:50 (Santa Cruz); monoclonal mouse anti-BrdU Antibody (IIB5) at 1:400 (Santa Cruz); and monoclonal mouse anti-c-Myc Antibody (9E10) at 1:400 (Santa Cruz).

Secondary antibodies (all at 1:400 dilution): donkey anti-rabbit IgG Alexa fluor 488, 594 and 647, donkey anti-mouse IgG Alexa fluor 488, 555, 594 and 647, donkey anti-goat IgG Alexa fluor 488 (Thermo Fisher).

For EdU-BrdU labelled chromosomes, spread chromosome samples were incubated with 1 M HCl for 10 min on ice and with 2 M HCl for 10 min at room temperature, and then neutralized with phosphate/citric acid buffer (0.2 M Na_2HPO_4, 0.1 M citric acid, pH 7.4) for 10 min at room temperature. After washing and blocking, cells were incubated with BrdU antibodies diluted in 5% BSA in PBST for 1 hr. Incorporated F-ara-EdU was detected with Alexa Fluor™ 488 Azide by Click-iT EdU imaging kits.

Imaging and Data Collection

Fixed samples imaging. Fixed samples were imaged in one of three different ways:

- Samples in Figures 1E, 2A, 3H, 3I, 4E, S2G, S3E and S4B were imaged with Structured Illumination Microscopy (SIM) using a 100x/1.4 NA Plan-Apochromat objective on an Elyra PS.1 microscope (Carl Zeiss). Fluorescence excitation was provided by 405, 488 and 561 nm diode lasers and an Andor EMCCD 1024 x 1024-pixel camera was used for detection. Stripe-based SIM illumination was utilized. Stripes were moved laterally five times at five different angles (rotations). Stage movement in Z was performed using a Z-Piezo system. Three-dimensional images were acquired with a raw voxel size of 0.05 x 0.05 x 0.08 µm and an updated voxel size of 0.03 x 0.03 x 0.08 µm after processing. Raw data was processed using Zeiss' ZEN Black software version 2.6.
- Samples in Figures 1F, 3B, 3D-3F, 4G, 4H, 6G-6I, 7E, 7F, S1B, S1C, S2D-2F, S4A middle bottom and S4C bottom were imaged with a LSM880 confocal microscope equipped with an Airyscan detector (Carl Zeiss) A 63x/1.4 NA Plan-Apochromat objective was used. Excitation light was from a 405 nm diode laser, 488 nm Argon laser or a 561 nm DPSS laser. Fluorescence was detected via the Zeiss Airyscan 32-channel GaAsP PMT array detector in super-resolution (SR) mode. Three-dimensional images were acquired in LineSequential Scan mode for single channel imaging, in Frame Scan model for two channels imaging, with 16 Bit depth and a raw voxel size 0.04 x 0.04 x

0.19 µm. The picture voxel sizes were the same after processing. Raw data was processed using Zeiss' ZEN Black software version 2.6.

- Images in Figures 2D, 2E, 3G, 4D, 6A, 6D and S2H, S3D and S4A (except middle bottom) were taken with an inverted Nikon Ti wide field epi-fluorescence microscope. Images in Figures 6E and S4D were collected using a Zeiss Axioplan IEmot confocal microscope. Images were collected using MetaMorph (Molecular Devices). Images were subjected to 1x deconvolution except Figures 2D, 2E, 6A, 6D and S4A (10x) and 6E and S4D (20x).

Live-cell Imaging. Cells were cultured on poly-lysine coated glass-bottom dishes (MatTek), FluoroBrite DMEM without phenol red (Life Technologies) with 10% FBS, 2 mM L-glutamine and 100 units/ml penicillin plus 100 mg/ml streptomycin.

Snapshots (Figures 1D, 3A, 3C, 4B, 4C, 2B, S1A, S2A, S2C, S2I, S3B, S3C and S4C top) and real-time imaging (Figures 5A-5E, S7A, S7C, S8, S9A and S9B) of living cells were performed with the LSM880+Airyscan confocal microscope described above. Samples were placed in a heated stage-top incubator (37°C) that was continually flooded with humidified air that was pre-warmed (37°C) and mixed with 5% CO_2. Further, the upper portion of the microscope stand was enclosed in a heated plexiglass chamber (37°C). Images were acquired at 30 sec, 5 min or other intervals or snapshots.

All raw data for the above experiments was processed using Zeiss' ZEN Black software version 2.6.

DM87 DNA live cell snapshot pictures (Figures 4A, 4B and S3A) and the LLC-Pk EGFP-TopIIα images in Figures 6E and S4D were taken on a Nikon-Ti inverted microscope equipped with a 100x/1.4NA oil emersion objective, Prior Lumen 200 excitation source, Nikon PerfectFocus system to eliminate Z drift, and an Andor Cascade II EMCCD camera. Z stacks were collected using a Prior NanoScanZ Nanopositioning Piezo Z Stage System. Slice separation ranged from 200 nm with 100–300 ms exposure time per slice, and typically covered a range of 20 µm. Samples were placed in a heated

stage-top incubator (37°C) that was continually flooded with humidified air that was pre-warmed (37°C) and mixed with 5% CO2. Slice separation ranged from 200 nm with 100–300 ms exposure time per slice, and typically covered a range of 20 µm for mammalian cells. Cells were incubated in DMEM with 0.1 µg/ml Hoechst 33342 for 5 min, washed three times with medium prior to imaging as (Liang et al., 2015). The pictures are deconvolved 1x iteration using AutoQuant (Media Cybernetics, Inc.) with appropriate point spread functions.

Image Analysis and Presentation. ***Channel alignment.*** Channel alignment in three fluorescence channels was implemented using 0.5 µm diameter multi-color beads (ThermoFisher). Beads were sonicated and dried onto a slide. Images taken in DAPI, FITC, and Cy3 channels were co-aligned using ZEN channel alignment software (Carl Zeiss).

Z direction correction. Z direction correction was performed using 0.5 µm diameter multi-color beads. In one approach, inter-plane distance was adjusted using the appropriate PSF. In a second approach, the 3D bead image was created using Image J and the inter-plane distance was adjusted manually until the diameter of the bead was the same in the Z dimension as in the X and Y dimensions. The same correction factor emerged by both methods.

3D renderings. All 3D renderings of whole axis and chromatin shapes and/or their centroids in Figures 6 and 7 were accomplished in PyMOL (http://www.pymolwiki.org/index.php/Tiff2ccp4; D. Jeruzalmi and J. Vertrees). For whole shapes, the visualized object is an iso-intensity surface contour that defines the volume encompassing signals whose signals are at or above a defined threshold. Renderings in Figures 5A, 5B, S7A and S7B) were performed with Volocity (PerkinElmer).

Measurement of Distances

Inter-bridge distances, inter-bubble distances and bubble sizes (Figures 2C, 2F and Figure S5). Inter-bridge distances (e.g. A-D below). Distances between TopIIα bridges were determined in fixed, spread preparations, in fixed whole cells and in living whole cells. Repesentative examples are shown for post-prophase (A-C) and late prophase (D). In fixed and living whole cells, chromosome examples selected for analysis were co-planar with the XY imaging plane and measurements were made from the middle single plane image of a 3D z-stack. For each chromosome, using Fiji, a line was drawn (yellow in panels (A-C; green/orange in (D)) by hand along the region between the two chromatids and the intensity profile along the line defined. Along this profile, the positions of peaks were defined, and the distances (in microns) between adjacent peaks determined, by the peakfinding function (findpeaks.m) from MatLab: https://www.mathworks.com/help/signal/ref/findpeaks.html. Distances between bridges as defined by DNA or chromatin staining were determined analogously.
Distances between bubbles and bubble lengths were determined from the same types of preparations as for bridges. The indicated lines (e.g. E and F below) were drawn by eye and then measured using Fiji.

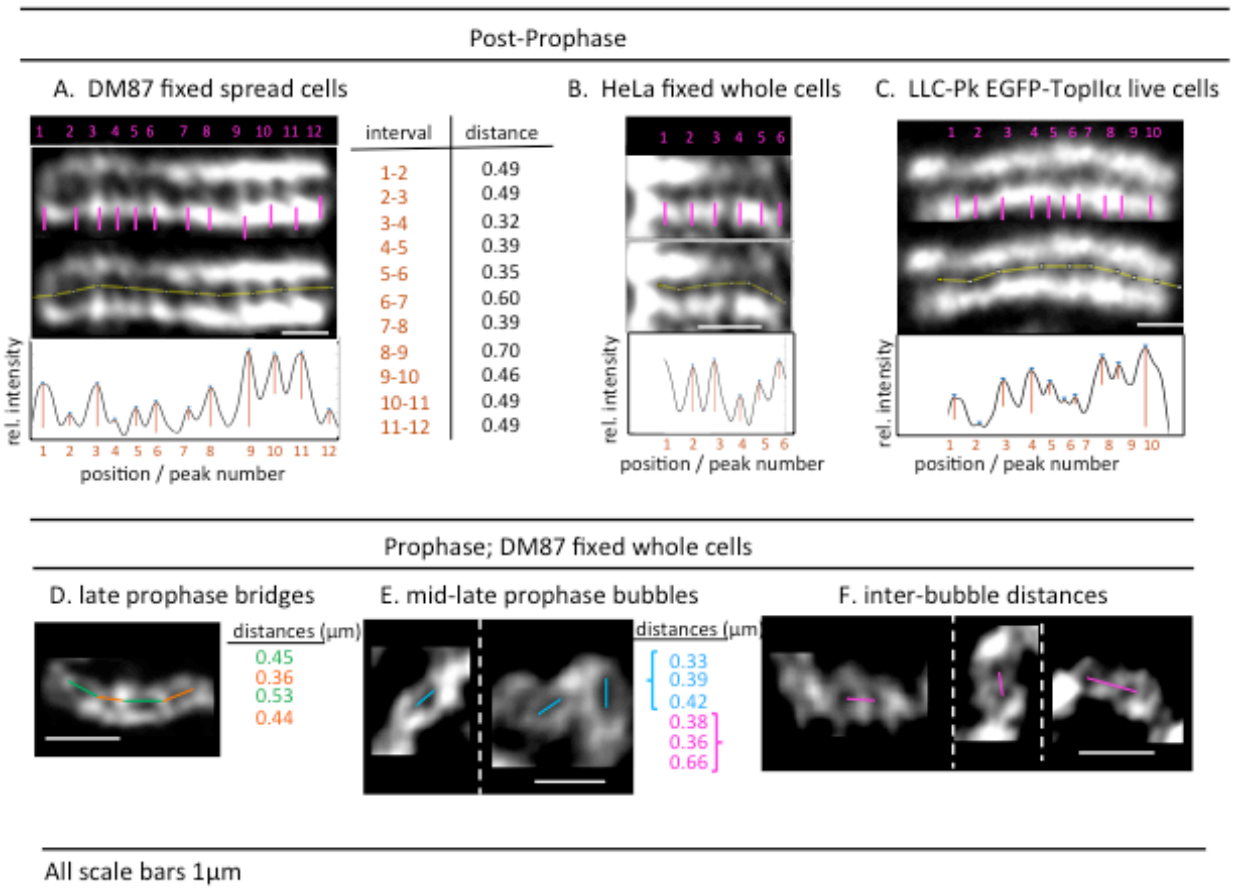

Inter-axis distances (Figures S8C and S8E). For a single mid-plane image from a 3D z-stack (S8C) or the single plane of a videomicrograph (S8E), a straight line is drawn by eye perpendicular to the longitudinal axes of the two chromatids. The lengths of these traces were measured in ImageJ software.

Determination of centroid paths. The centroid paths of chromosome axis shapes and chromatin shapes (Figures 6I-6L, 7A and S6C) were defined with a home-made algorithm that uses an intensity-weighted centroid computation.

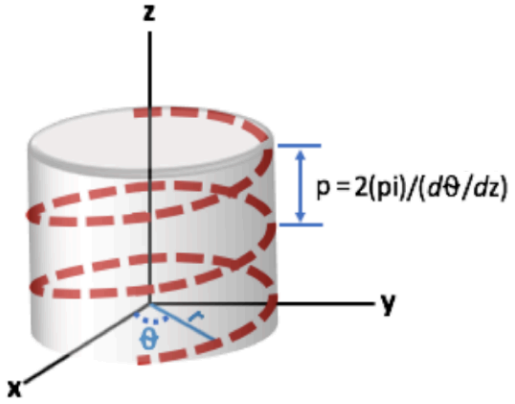

First, candidate objects in the imaged volume are segmented from adjacent objects and each object is rotated so that its major axis is aligned in the z-direction. The software then segments the object

slice-by-slice calculates the centroid for each slice. The unit of distance from slice to slice in the z-direction is the same as the dimension of one pixel in the input image. A minimum Euclidean distance filter then spatially links the centroid across slices.

One end of the centroid path (shown as the "bottom" below) is then assigned as the local origin, and centroid locations are converted to the cylindrical coordinate system, (r,q,z), which provides a convenient way to reference changes in pitch and handedness. In this coordinate system, z is the distance along the major axis, while r and θ are lateral and angular displacements from the local origin, respectively.

Here, pitch p is defined as the distance in z over which changes in θ accumulate to 2π radians. Because the change in angle is in the denominator, the pitch measurement is sensitive to noise which presents itself as small-scale, large magnitude swings in value. A smoothing Gaussian derivative is used when calculating pitch, where the smoothing scale t is equivalent to the variance of the smoothing Gaussian. This means that any changes in pitch larger than $1/\sqrt{t}$ are smoothed away.

Changes in sign/zero-crossings in $d\theta/dz$ provides information about the handedness in the helical tendency of the object centroid. The consequences of using the smoothing factor t means that the algorithm is insensitive to the location of changes in handedness at length scales smaller than $\sqrt{t}$. Since t is measured in pixels, the corresponding insensitivity in length will depend on scale calibration on the axis over which the centroid major axis was aligned. The Gaussian smoothing “smears” out uncertainty in the location of the change in handedness, with the uncertainty being equal to 2*sqrt(t). All centroid paths analyzed in the current study were defined with Gaussian smoothing function t=1 that allows to remove small-scale, large magnitude spikes in $d\theta/dz$ related to noise. Importantly, the results are not critically dependent on this value: nearly identical patterns are obtained with smoothing function values of t=0.1 to 2.

Analysis of axis centroid paths

Contour lengths of handedness segments (Figures 6M and 7B). Contour length of a segment of given handedness is given by the corresponding the number of slices as defined by the algorithm, multiplied by the size of the pixel in the image (above).

Comparison of left- and right-handedness lengths (Figure S6B) was made by summing the total number of slices (pixels) of each handedness for the centroid paths of the desired group of axis images.

Comparison of handednesses between split sister axes of late leptotene axes (Figure S6A). For each late leptotene chromosome, the centroid paths of sister axes were phased by eye. Then, for each corresponding slice (pixel) position, handedness comparisons were defined as both R, both L, or different (RL or LR) and the totals for each category presented.

Comparison of curvature for mid-prophase and late prophase centroid paths (Figure 7C). Centroid paths are given as list of x, y and z coordinates with every point of the path defined as $\mathbf{P}_i = [x_i, y_i, z_i]$. The circle passing through all three corners of the triangle formed by the neighboring points $\mathbf{P}_{i-n}$, $\mathbf{P}_i$ and $\mathbf{P}_{i+n}$ is used to calculate the curvature at $\mathbf{P}_i$, n being a distance from $\mathbf{P}_i$ in pixels. $\boldsymbol{M_i}$ is the center and R_i is the radius of this circle. The curvature of the path at $\boldsymbol{P}_i$ is defined as $\kappa_i = 1/R_i$. The curvature vector $\mathbf{k}_i$ is defined as the vector of length κ_i in the direction from $\mathbf{P}_i$ to $\boldsymbol{M_i}$. κ_i were calculated at every point of mid-prophase and late prophase centroid paths using an adaptation of Matlab script (Mjaavatten, 2019) and plotted as histograms normalized with probability density function.

STATISTICAL ANALYSIS. *Gamma fitting analysis* (Figures 2C and 2F). Distance and length distributions were plotted with Matlab 2018a (The MathWorks, Inc). Distributions were fitted with a gamma function from the 99% confidence interval. The data means and their standard deviations were calculated with Matlab. For each of the distributions, the values of the data mean and the shape parameter from the gamma fit are shown.

DATA AND SOFTWARE AVAILABILITY

Software Availability. The program for centroid path determination and analysis, written in MATLAB, is available at https://projects.iq.harvard.edu/kleckner_lab/lab-software

1182

VIDEOS

Video 1. Prophase to anaphase in living Haemanthus chromosomes. (Inoue and Oldenbourg, 1998; doi mk0780643001)

Video 2. 3D rendering of axis and chromatin centroids for the chromosome in Figure 6J.

Video 3. 3D rendering of unsplit prophase chromosome pictured in Figure 6G-I and Figure 6J(i). First half of movie shows axis and chromatin centroids of Figure 6J(i). Second half of movie shows these centroids embedded in the corresponding whole axis and chromatin shapes as shown in Figure 6I.

Video 4. 3D rendering of axis shape and its centroid for unsplit prophase chromosome pictured in Figure 7A, left top.

Video 5. 3D rendering of axis shape and its centroid for split late prophase chromosome pictured in Figure 7A, middle/bottom left.

REFERENCES

Booth, D.G., Beckett, A.J., Molina, O., Samejima, I., Masumoto, H., Kouprina, N., Larionov, V., Prior, I.A., and Earnshaw, W.C. (2016). 3D-CLEM Reveals that a Major Portion of Mitotic Chromosomes Is Not Chromatin. Mol. Cell *64*, 790-802.

Cremer, T. and Cremer, M. (2010). Chromosome Territories. Cold Spring Harbor Perspect. Biol. *2: a003889.*

Farcas, A-M., Uluocak, P., Helmhart, W. and Nasmyth, K. (2011). Cohesin's Concatenation of Sister DNAs Maintains Their Intertwining. Mol. Cell *44*, 97-107.

Gerbode, S.J., Puzey, J.R., McCormick, A.G., and Mahadevan, L. (2012). How the cucumber tendril coils and overwinds. Science *337*, 1087-1091.

Gibcus, J.H., Samejima, K., Goloborodko, A., Samejima, I., Naumova, N., Nuebler, J., Kanemaki, M.T., Xie, L., Paulson, J.R., Earnshaw, W.C., Mirny, L.A., and Dekker, J. (2018). A pathway for mitotic chromosome formation. Science *359*, eaao6135.

Giménez-Abián, J.F., Clarke, D.J., Mullinger, A.M., Downes, C.S., and Johnson, R.T. (1995). A postprophase topoisomerase II-dependent chromatid core separation step in the formation of metaphase chromosomes. J Cell Biol. *131*, 7-17.

Giménez-Abián, J.F., Clarke, D.J., Devlin, J., Giménez-Abián, M.I., De la Torre, C., Johnson, R.T., Mullinger, A.M., and Downes, C.S. (2000). Premitotic chromosome individualization in mammalian cells depends on topoisomerase II activity. Chromosoma *109*, 235-44.

Giménez-Abián, J.F., Sumara, I., Hirota, T., Hauf, S., Gerlich, D., De la Torre, C., Ellenberg, J., and Peters, J.M. (2004). Regulation of sister chromatid cohesion between chromosome arms. Curr. Biol. *14*, 1187-93.

Gómez, R., Jordan, P.W., Viera, A., Alsheimer, M., Fukuda, T., Jessberger, R., Llano, E., Pendás, A.M., Handel, M.A., and Suja, J.A. (2013). Dynamic localization of SMC5/6 complex proteins during mammalian meiosis and mitosis suggests functions in distinct chromosome processes. J Cell Sci. *126*, 4239-52.

Goyal, S., Perkins, N.C., and Lee, C.L. (2005). Nonlinear dynamics and loop formation in Kirchhoff rods with implications to the mechanics of DNA and cables. Journal of Computational Physics *209*, 371-389.

Goyal, S., Todd, L., Perkins, N.C., and Meyhofer, E. (2007). Cable dynamics applied to long length-scale mechanics of DNA. arXiv:physics/0702197

Grinthal, A., Adamovic, I., Weiner, B., Karplus, M., and Kleckner, N. (2010). PR65, the HEAT-repeat scaffold of phosphatase PP2A, is an elastic connector that links force and catalysis. Proc. Natl. Acad. Sci. USA *107*, 2467-2472.

Groves, M.R. and Barford, D. (1999). Topological characteristics of helical repeat proteins. Curr. Opin. Struct. Biol. *9*, 383-389.

Halatek, J., Brauns, F., and Frey, E. (2018). Self-organization principles of intracellular pattern formation. Philos. Trans. R. Soc. Lond. B. Biol. Sci. *373*, 20170107.

Hauf, S., Waizenegger, I.C., and Peters, J.M. (2001). Cohesin cleavage by separase required for anaphase and cytokinesis in human cells. Science *293*,1320-1323.

Houchmandzadeh, B., and Dimitrov, S. (1999). Elasticity measurements show the existence of thin rigid cores inside mitotic chromosomes. J. Cell Biol. *145*, 215-223.

Houchmandzadeh B, Marko JF, Chatenay D, Libchaber A. (1997). Elasticity and structure of eukaryote chromosomes studied by micromanipulation and micropipette aspiration. J Cell Biol. *139*, 1-12.

Inoué, S. and Oldenbourg, R. (1998). Microtubule dynamics in mitotic spindle displayed by polarized light microscopy. Mol. Biol. Cell *9*, 1603-1607.

Jane, F.W. (1934). The structure of somatic chromosomes of Alstromeria and Bomarea. J. Cell SCi *s2-77*: 49-75

Kirchhoff, G. (1859). Uber das Gleichgewicht und de Bewegung eines unendlich dunnen elastischen Stabes. J. Mathematik (Grelle) *56*, 285-313.

Kleckner N, Zickler D, Jones GH, Dekker J, Padmore R, Henle J, Hutchinson J. (2004) A mechanical basis for chromosome function. Proc Natl Acad Sci U S A. *101*:12592-7.

Kops, G.J., van der Voet, M., Manak, M.S., van Osch, M.H., Naini, S.M., Brear, A., McLeod, I.X., Hentschel, D.M., Yates, J.R.3rd., van den Heuvel, S., and Shah, J.V. (2010). APC16 is a conserved subunit of the anaphase-promoting complex/cyclosome. J. Cell Sci. *123*,1623-1633.

Ku, Torii (2012). Two-dimensional spatial patterning in developmental systems. Trends Cell. Biol. *22*, 438-446.

Lebofsky, R., Heilig, R., Sonnleitner, M., Weissenbach, J., and Bensimon, A. (2006). DNA replication origin interference increases the spacing between initiation events in human cells. Mol. Biol. Cell *17*, 5337-5346.

Liang, Z., Zickler, D., Prentiss, M., Chang, F.S., Witz, G., Maeshima, K., and Kleckner, N. (2015). Chromosomes Progress to Metaphase in Multiple Discrete Steps via Global Compaction/Expansion Cycles. Cell *161*, 1124-1137.

Liu, J., Huang, J., Su, T., Bertoldi, K., and Clarke, D.R. (2014). Structural transition from helices to hemihelices. PLoS One. *9*, e93183.

Llères, D., James, J., Swift, S., Norman, D.G., and Lamond, A.I. (2009). Quantitative analysis of chromatin compaction in living cells using FLIM-FRET. J. Cell Biol. 16, 481-496.

Love, A.E.H. (1927). A treatise on the mathematical theory of elasticity (4th Edition, Cambridge University Press).

Maeshima, K. and Laemmli, U.K. (2003). A two-step scaffolding model for mitotic chromosome assembly. Dev. Cell *4*, 467-80.

Maeshima, K., Imai, R., Tamura, S., and Nozaki, T. (2014). Chromatin as dynamic 10-nm fibers. Chromosoma *123*, 225-237.

Manders, E.M., Kimura, H., and Cook, P.R. (1999). Direct imaging of DNA in living cells reveals the dynamics of chromosome formation. J. Cell Biol. *144*, 813–821.

Marko, J.F. and Siggia, E.D. (1997). Polymer models of meiotic and mitotic chromosomes. Mol. Biol. Cell *8*, 2217-2231.

Marko, J.F. and Poirier, M.G. (2003). Micromechanics of chromatin and chromosomes. Biochem. Cell Biol. *81*, 209-20.

Marsden, M.P. and Laemmli, U.K. (1979). Metaphase chromosome structure: evidence for a radial loop model. Cell *17*, 849-58.

Mizuuchi, K. and Vecchiarelli, A.G. (2018). Mechanistic insights of the Min oscillator via cell-free reconstitution and imaging. Phys. Biol. *15*, 031001.

Mjaavatten, A. (2019). Curvature of a 2D or 3D curve. (https://www.mathworks.com/matlabcentral/fileexchange/69452-curvature-of-a-2d-or-3d-curve), MATLAB Central File Exchange.

Nagasaka, K., Hossain, M.J., Roberti, M.J., Ellenberg, J., and Hirota, T. (2016). Sister chromatid resolution is an intrinsic part of chromosome organization in prophase. Nat. Cell Biol. *18*, 692-9.

Nakajima M, Kumada K, Hatakeyama K, Noda T, Peters JM, Hirota T. (2007) The complete removal of cohesin from chromosome arms depends on separase. J Cell Sci. *120*:4188-96.

Natsume, T., Kiyomitsu, T., Saga, Y., and Kanemaki, M.T. (2016). Rapid Protein Depletion in Human Cells by Auxin-Inducible Degron Tagging with Short Homology Donors. Cell Rep. *15*, 210-218.

Neef, A.B., and Luedtke, N.W. (2011). Dynamic metabolic labeling of DNA in vivo with arabinosyl nucleosides. Proc. Natl. Acad. Sci. USA *108*, 20404-20409.

Neumann, B., Walter, T., Hériché, J.K., Bulkescher, J., Erfle, H., Conrad, C., Rogers, P., Poser, I., Held, M., Liebel, U., Cetin, C., Sieckmann, F., Pau, G., Kabbe, R., Wünsche, A., Satagopam, V., Schmitz, M.H., Chapuis, C., Gerlich, D.W., Schneider, R., Eils, R., Huber, W., Peters, J.M., Hyman, A.A., Durbin, R., Pepperkok, R., and Ellenberg, J. (2010). Phenotypic profiling of the human genome by time-lapse microscopy reveals cell division genes. Nature *464*, 721-727.

Neuwald, A.F. and Hirano, T. (2000). HEAT repeats associated with condensins, cohesins, and other complexes involved in chromosome-related functions. Genome Res. *10*, 1445-52.

Ono, T., Fang, Y., Spector, D.L., and Hirano, T. (2004). Spatial and temporal regulation of Condensins I and II in mitotic chromosome assembly in human cells. Mol. Biol. Cell *15*, 3296-308.

Piskadlo, E., Tavares, A. and Oliveira, R.A. (2017). Metaphase chromosome structure is dynamically maintained by condensin I-directed DNA (de)catenation. Elife *6,* e26120.

Poirier, M.G. and Marko, J.F. (2002). Mitotic chromosomes are chromatin networks without a mechanically contiguous protein scaffold. Proc. Natl. Acad. Sci. USA *99*, 15393-15397.

Schindelin, J., Arganda-Carreras, I., Frise, E., Kaynig, V., Longair, M., Pietzsch, T., Preibisch, S., Rueden, C., Saalfeld, S., Schmid, B., et al. (2012). Fiji: an open-source platform for biological-image analysis. Nat. Methods *28*, 676–682.

Skibbens, R.V. (2019). Condensins and cohesins - one of these things is not like the other! J. Cell Sci. *132*, jcs220491.

Tavormina, P.A., Côme, M.G., Hudson, J.R., Mo, Y.Y., Beck, W.T., and Gorbsky, G.J. (2002). Rapid exchange of mammalian topoisomerase II alpha at kinetochores and chromosome arms in mitosis. J. Cell Biol. 158, 23-29.

Turing, A.M. (1952). The Chemical Basis of Morphogenesis. Philosophical Transactions of the Royal Society of London. Series B, Biological Sciences *237*, 37-72.

Vassilev, L.T., Tovar, C., Chen, S., Knezevic, D., Zhao, X., Sun, H., Heimbrook, D.C., Chen, L. (2006). Selective small-molecule inhibitor reveals critical mitotic functions of human CDK1. Proc. Natl. Acad. Sci. USA *103*, 10660-10665.

Wang, J.C. (2002). Cellular roles of DNA topoisomerases: a molecular perspective. Nat. Rev. Mol. Cell Biol. *3*, 430-40.

Wang, J.C. and Cozzarelli, N.R. (1990) DNA Topologiy and Its Biological Effects.

Yoshimura, S.H. and Hirano, T. (2016). HEAT repeats - versatile arrays of amphiphilic helices working in crowded environments? J. Cell Sci. *129*, 3963-3970.

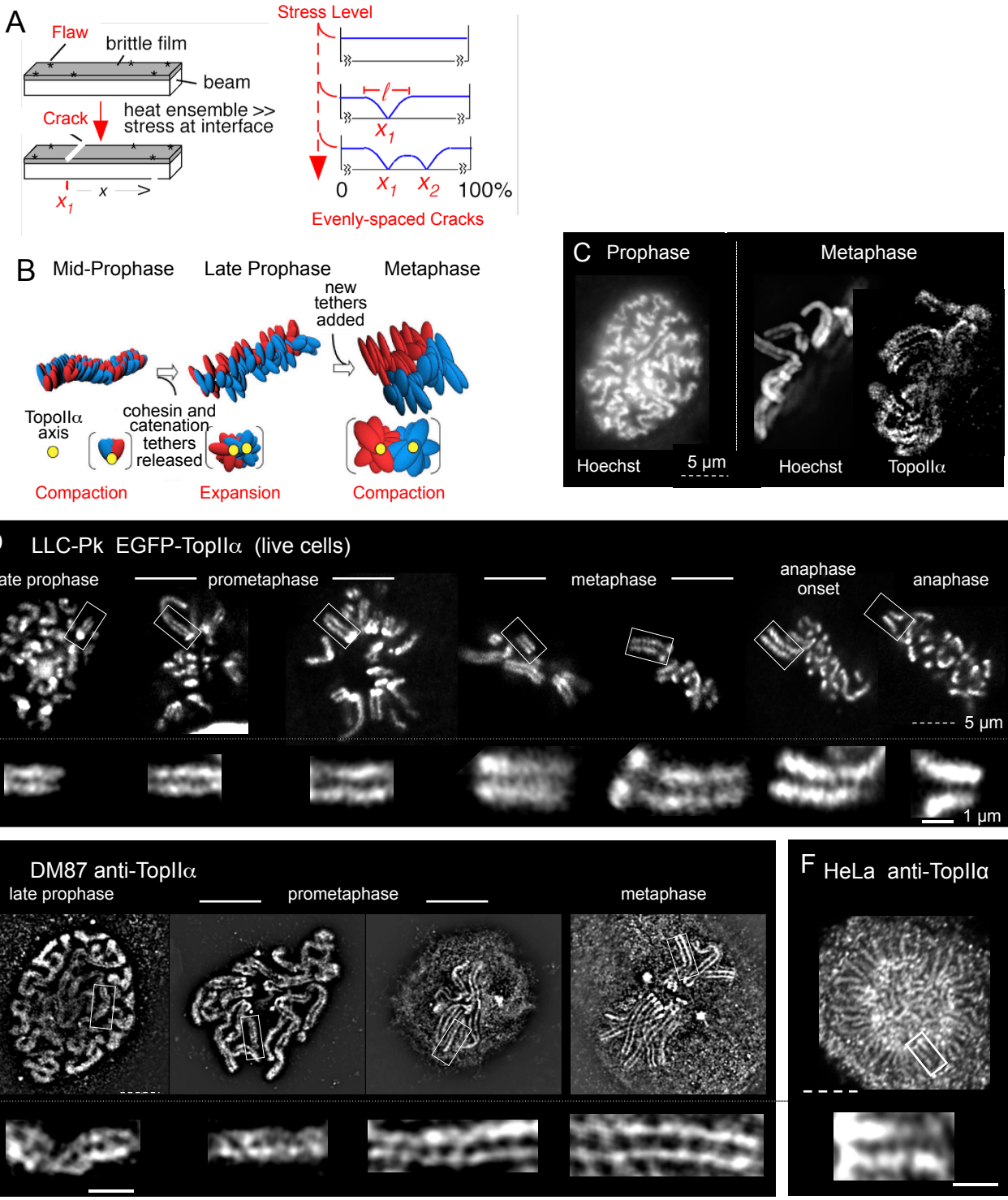
A
Flaw
brittle film
beam
Crack
heat ensemble >>
stress at interface
x
x1
Stress Level
l
x1
0
x1
x2
100%
Evenly-spaced Cracks
B
Mid-Prophase
Late Prophase
Metaphase
new
tethers
added
TopoIIα
axis
cohesin and
catenation
tethers
released
Compaction
Expansion
Compaction
C
Prophase
Metaphase
Hoechst
5 μm
Hoechst
TopoIIα
D
LLC-Pk EGFP-TopIIα (live cells)
late prophase
prometaphase
metaphase
anaphase
onset
anaphase
5 μm
1 μm
E
DM87 anti-TopIIα
late prophase
prometaphase
metaphase
F
HeLa anti-TopIIα

Figure 1

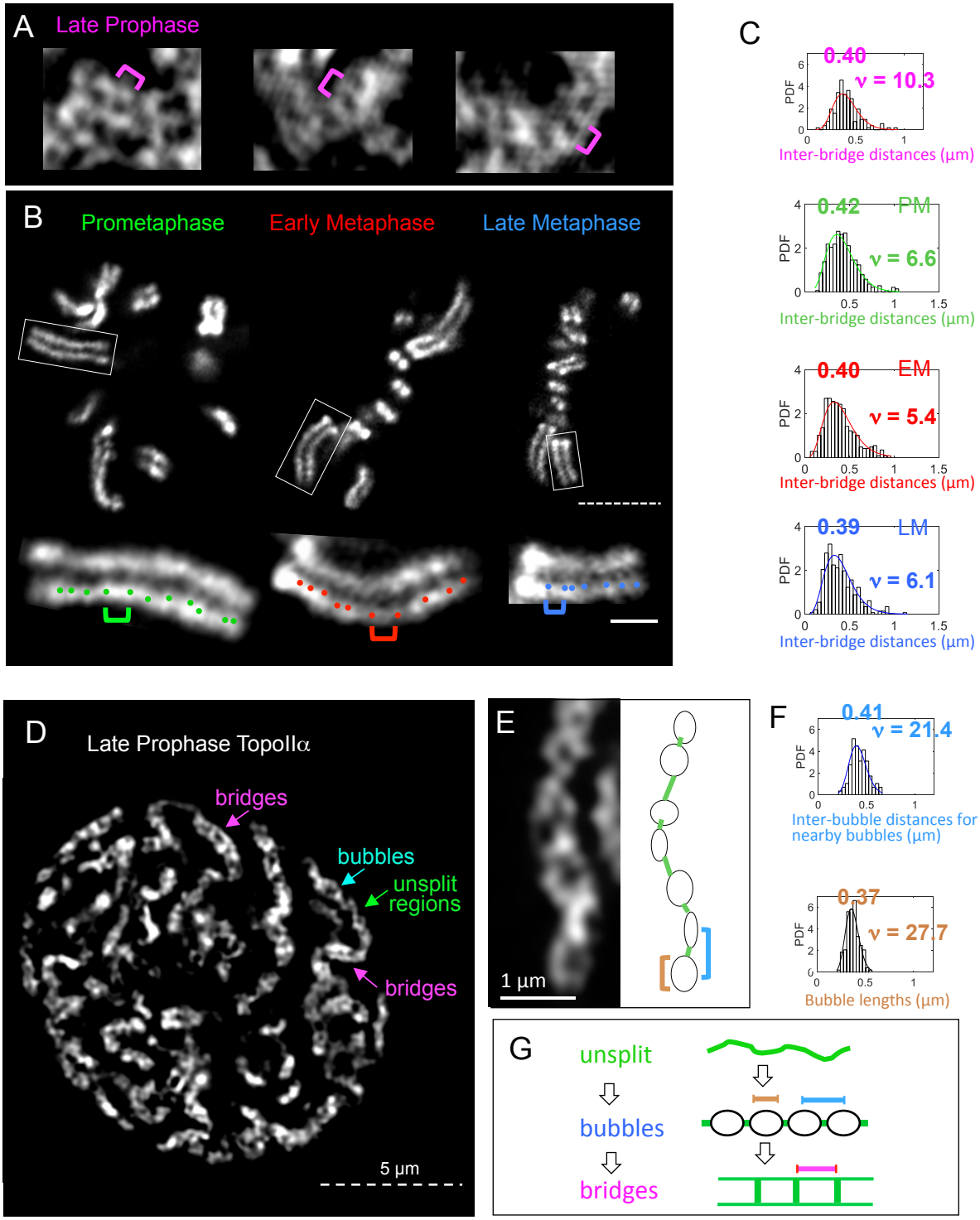
A
Late Prophase
B
Prometaphase
Early Metaphase
Late Metaphase
C
0.40
ν = 10.3
PDF
Inter-bridge distances (μm)
0.42
PM
ν = 6.6
Inter-bridge distances (μm)
0.40
EM
ν = 5.4
Inter-bridge distances (μm)
0.39
LM
ν = 6.1
Inter-bridge distances (μm)
D
Late Prophase TopoIIα
bridges
bubbles
unsplit regions
bridges
5 μm
E
1 μm
F
0.41
ν = 21.4
Inter-bubble distances for nearby bubbles (μm)
0.37
ν = 27.7
Bubble lengths (μm)
G
unsplit
bubbles
bridges

Figure 2

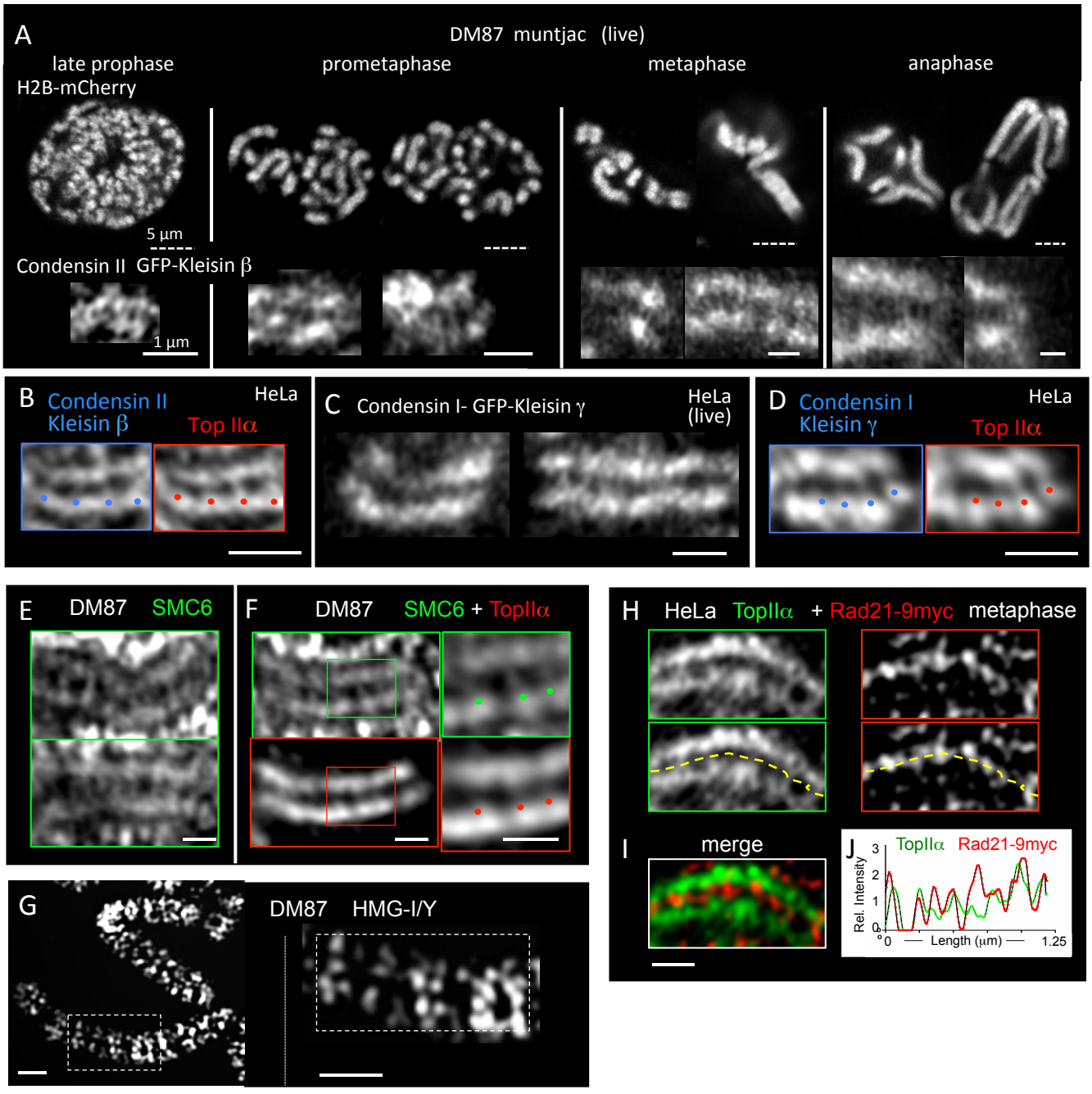
A
DM87 muntjac (live)
late prophase
prometaphase
metaphase
anaphase
H2B-mCherry
5 µm
Condensin II GFP-Kleisin β
1 µm
B
Condensin II
Kleisin β
Top IIα
HeLa
C
Condensin I- GFP-Kleisin γ
HeLa
(live)
D
Condensin I
Kleisin γ
Top IIα
HeLa
E
DM87 SMC6
F
DM87 SMC6 + TopIIα
G
DM87 HMG-I/Y
H
HeLa TopIIα + Rad21-9myc metaphase
I
merge
J
TopIIα Rad21-9myc
Rel. Intensity
Length (µm)
1.25

Figure 3

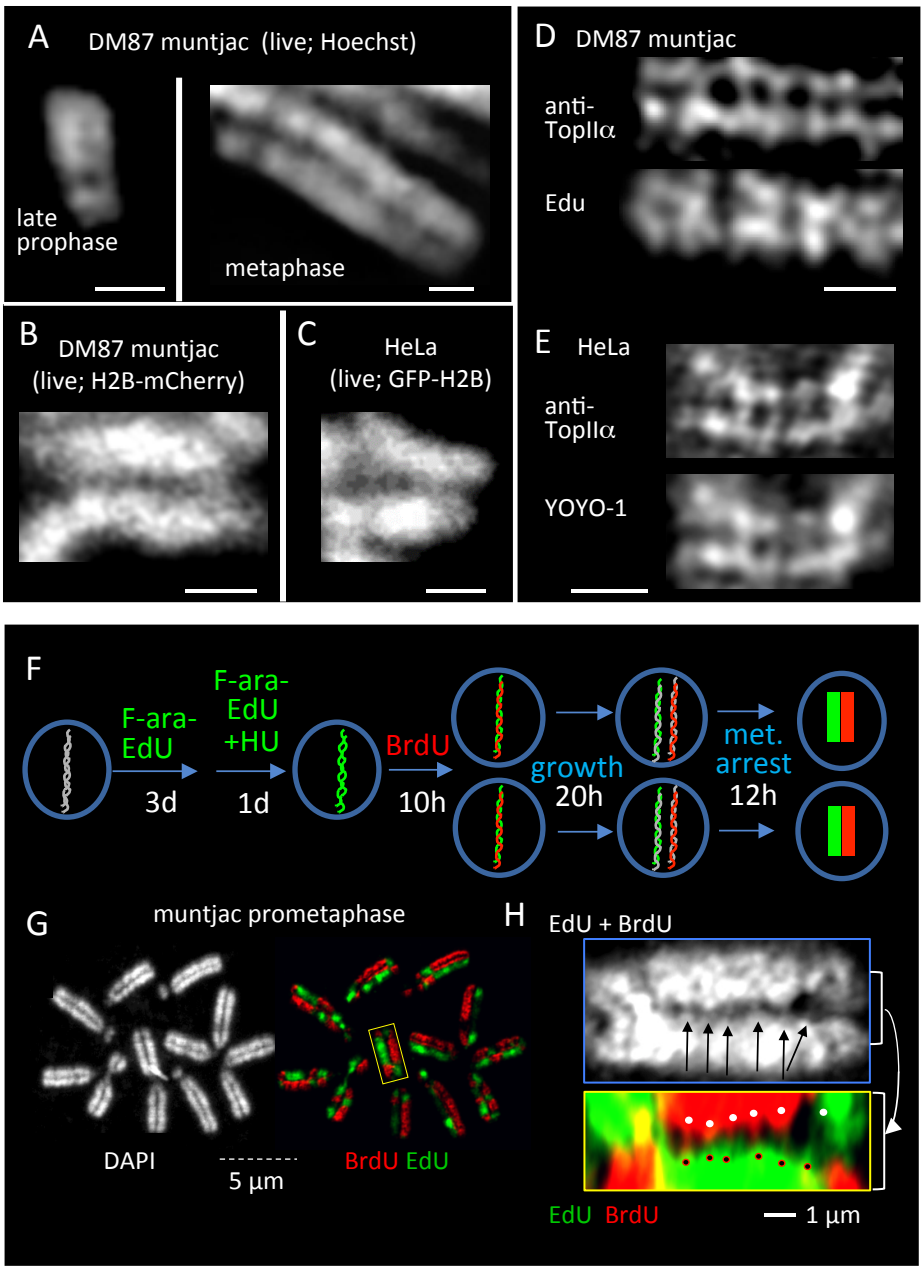
A
DM87 muntjac (live; Hoechst)
late prophase
metaphase
B
DM87 muntjac (live; H2B-mCherry)
C
HeLa (live; GFP-H2B)
D
DM87 muntjac
anti-TopIIα
Edu
E
HeLa
anti-TopIIα
YOYO-1
F
F-ara-EdU
3d
F-ara-EdU +HU
1d
BrdU
10h
growth
20h
met. arrest
12h
G
muntjac prometaphase
DAPI
5 µm
BrdU EdU
H
EdU + BrdU
EdU BrdU
1 µm
I
catenation of sister loops
J
TopoIIα; Condensins I, II; SMC5/6; HMG1/Y, cohesin

Figure 4

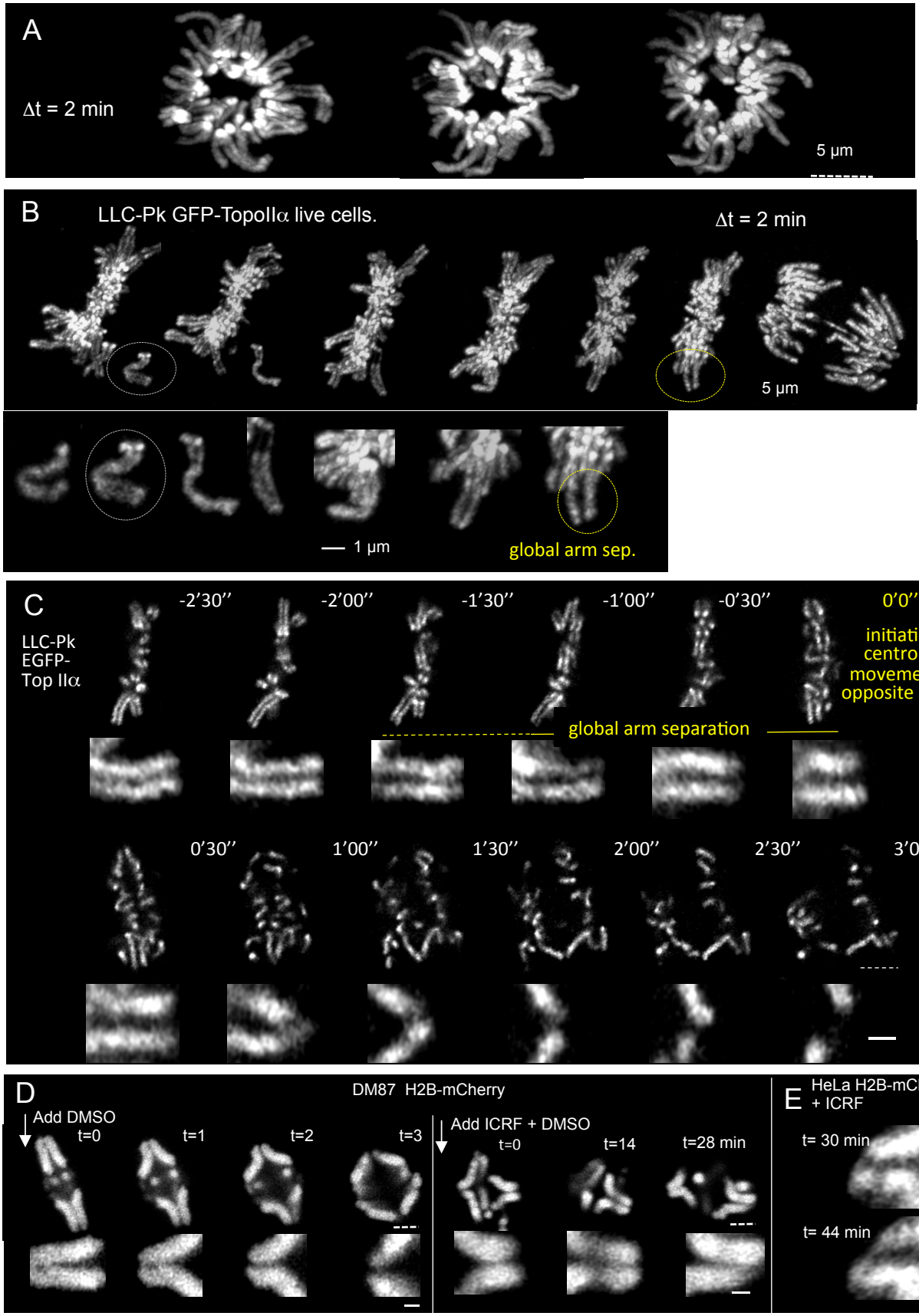
A
Δt = 2 min
5 μm
B
LLC-Pk GFP-TopoIIα live cells.
Δt = 2 min
5 μm
1 μm
global arm sep.
C
LLC-Pk
EGFP-
Top IIα
-2'30''
-2'00''
-1'30''
-1'00''
-0'30''
0'0''
initiation of centromere movement to opposite poles
global arm separation
0'30''
1'00''
1'30''
2'00''
2'30''
3'0''
D
DM87 H2B-mCherry
Add DMSO
t=0
t=1
t=2
t=3
Add ICRF + DMSO
t=0
t=14
t=28 min
E
HeLa H2B-mCherry
+ ICRF
t= 30 min
t= 44 min

Figure 5

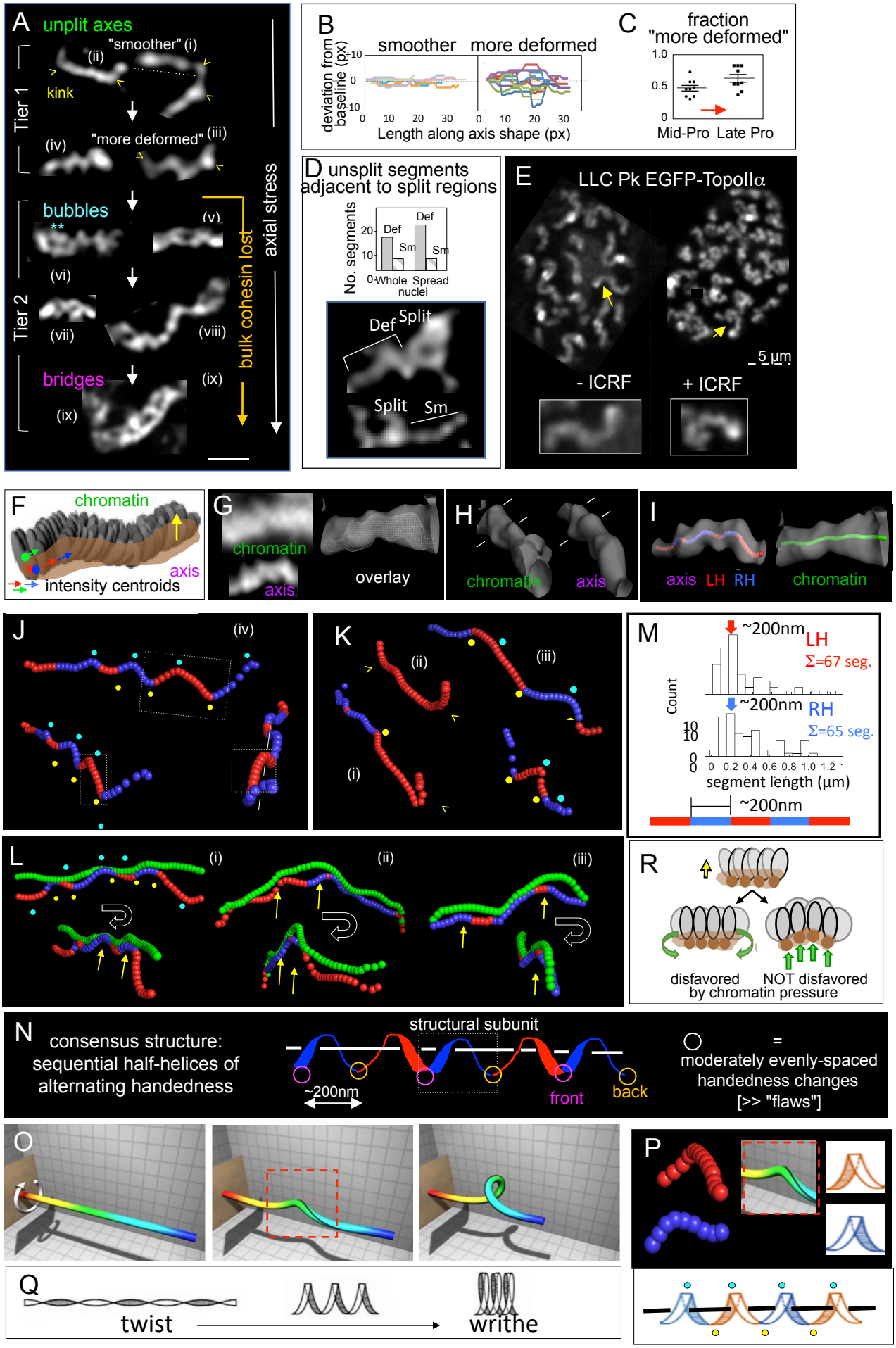
A
unplit axes
"smoother" (i)
(ii)
kink
Tier 1
(iv)
"more deformed" (iii)
bubbles
(v)
**
(vi)
Tier 2
(vii)
(viii)
bridges
(ix)
(ix)
bulk cohesin lost
axial stress
B
smoother
more deformed
deviation from baseline (px)
+10
0
-10
0 10 20 30 0 10 20 30
Length along axis shape (px)
C
fraction "more deformed"
1.0
0.5
0
Mid-Pro Late Pro
D unsplit segments adjacent to split regions
No. segments
20
10
0
Def
Sm
Def
Sm
Whole
Spread nuclei
Def
Split
Split
Sm
E
LLC Pk EGFP-TopoIIα
5 μm
- ICRF
+ ICRF
F
chromatin
axis
intensity centroids
G
chromatin
axis
overlay
H
chromatin
axis
I
axis
LH
RH
chromatin
J
(iv)
K
(ii)
(iii)
(i)
M
~200nm
LH
Σ=67 seg.
Count
~200nm
RH
Σ=65 seg.
10
10
0
0
0 0.2 0.4 0.6 0.8 1.0 1.2
segment length (μm)
~200nm
L
(i)
(ii)
(iii)
R
disfavored
NOT disfavored
by chromatin pressure
N
consensus structure:
sequential half-helices of
alternating handedness
structural subunit
~200nm
front
back
= moderately evenly-spaced handedness changes [>> "flaws"]
O
P
Q
twist
writhe

Figure 6

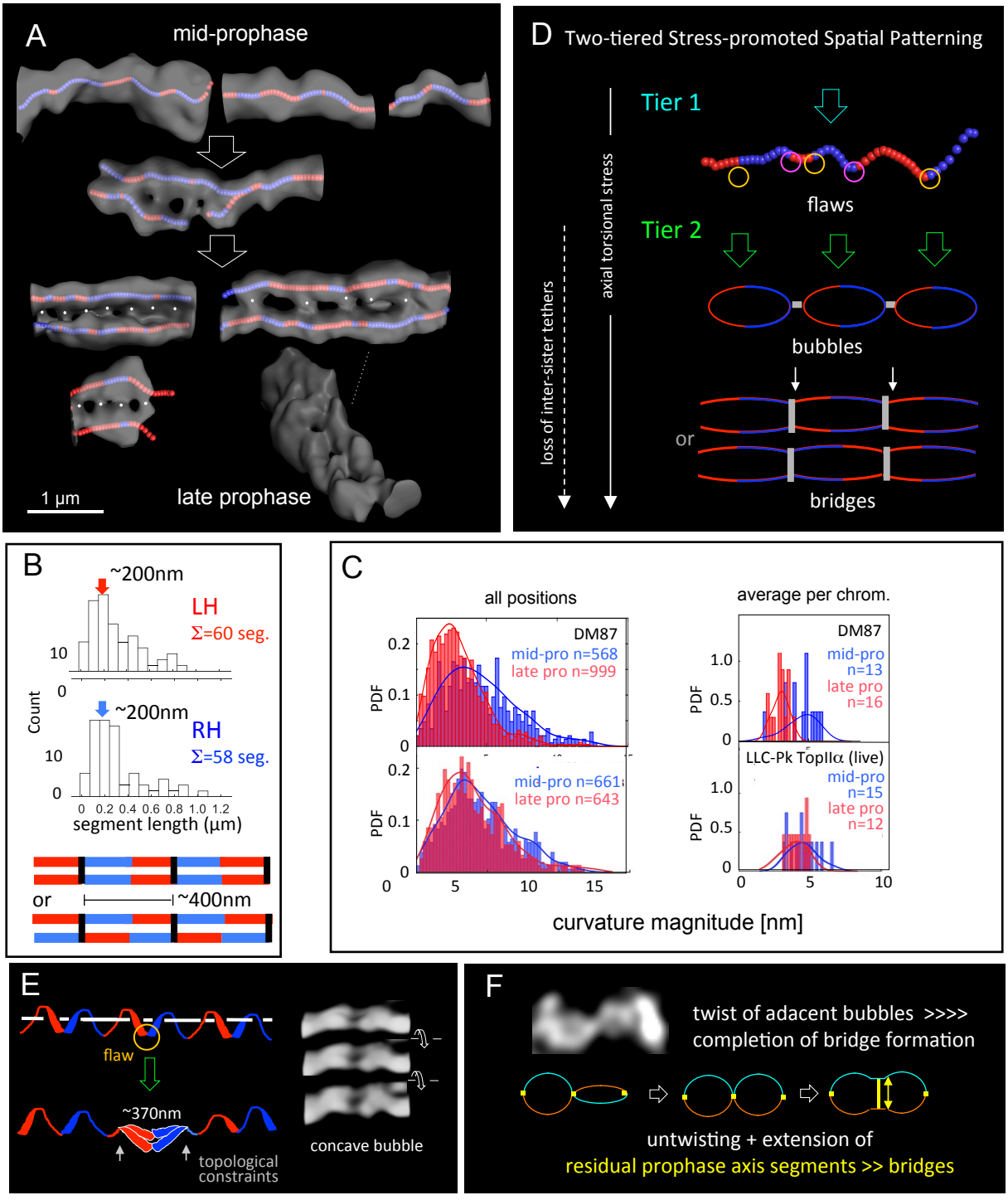
A
mid-prophase
1 µm
late prophase
D Two-tiered Stress-promoted Spatial Patterning
Tier 1
flaws
Tier 2
bubbles
or
bridges
axial torsional stress
loss of inter-sister tethers
B
~200nm
LH
Σ=60 seg.
~200nm
RH
Σ=58 seg.
Count
segment length (µm)
or
~400nm
C
all positions
average per chrom.
DM87
mid-pro n=568
late pro n=999
mid-pro n=661
late pro n=643
LLC-Pk TopIIα (live)
mid-pro n=15
late pro n=12
PDF
curvature magnitude [nm]
E
flaw
~370nm
topological constraints
concave bubble
F
twist of adacent bubbles >>>>
completion of bridge formation
untwisting + extension of
residual prophase axis segments >> bridges

Figure 7